Estuaries and Coasts
https://doi.org/10.1007/s12237-022-01156-9

The Bed Stress Minimum in Tidal Rivers

Austin Hudson[1] · David Jay[1] · Stefan Talke[2]

Received: 13 August 2022 / Revised: 22 November 2022 / Accepted: 2 December 2022

Abstract

Bed stress patterns control erosion and deposition in tidal rivers and thereby govern changes in geomorphology. Management of river discharge and shipping channel geometry perturbs rivers from their natural state, leading to hotspots of sand deposition and erosion. Here, we investigate the along-channel variability in bed stress for a tidal river of constant depth with semidiurnal tides and convergent geometry using a Fourier decomposition of the quadratic bed stress and analytical approximations of tidal and river velocity. Under some river discharge and tidal conditions, bed stress profiles exhibit a local bed stress minimum, x_{min}, within a region marked by strong gradients in cross-sectionally averaged velocity. These gradients can lead to convergent sediment fluxes and shoaling near x_{min}. Factors decreasing river velocity (flow management, channel deepening, and weak channel convergence) move x_{min} and depositional areas upstream. Analytical estimates of x_{min} were validated using fifty-two two-dimensional Adaptive Hydraulics (AdH) numerical model simulations and agree well with the sediment transport behavior of three prototype systems (Columbia River, Hudson River, and Delaware Estuary). Climate changes in seasonal flow cycles and mean river discharge, and the reservoir management response to these changes, may significantly alter the dynamics of x_{min}, affecting ecosystem dynamics and the stability of wetlands and coastal beaches as sea level rises. The analytical formulation of x_{min} developed herein will make it easier to understand how climate and human-induced changes to a river can impact long-term erosion/accretion patterns and can help guide future investments for managing sediment.

Keywords Bed stress · Tides · River flow · Sediment transport · Estuaries · Bed stress minimum

Introduction

This study analyzes along-channel variations in bed stress in tidal rivers to better understand what factors control system-scale shoaling and erosion patterns. Bed stress defines the amount of force per unit area imparted by the water on the riverbed and is an important consideration for informed sediment management practices because of its strong influence on the fate and transport of sediment (Dyer 1986). The cost of managing sediment highlights the need to better understand the processes controlling deposition in the tidal-fluvial environment. For example, every year the United States Army Corps of Engineers dredges roughly 200 million cubic yards of sediment, at a cost which has exceeded $1 billion annually since 2008 (USACE 2020). Much of this dredging is in estuaries and tidal rivers. Depositional regions can also contain elevated concentrations of legacy or emerging contaminants, which pose a risk to environmental and human health and could cost hundreds of millions of dollars to remediate (EPA 2014, 2016, 2017). Changes in tides, channel geometry, and

Communicated by Eduardo Siegle

Key Points

- Channel convergence and tidal attenuation in rivers may together produce a local minimum in the along-channel distribution of bed stress and a sediment convergence zone.
- The bed stress minimum contributes to channel shoaling, down-river fining of bed material, and seasonal sediment storage and limits littoral sediment supply.
- Channel deepening and flow reduction move the bed stress minimum upriver, which alters shoaling volume/composition and may also affect wetland stability.

✉ Austin Hudson
hudsona@pdx.edu

1 Civil and Environmental Engineering, Portland State University, Portland, OR, USA

2 Civil and Environmental Engineering, California Polytechnic State University, San Luis Obispo, CA, USA

Published online: 23 December 2022

river discharge can influence the magnitude and location of shoaling (Meade 1969; de Jonge et al. 2014; Bolla Pittaluga et al. 2015). Thus, improving practical knowledge of how the bed stress responds to adjustments in river discharge, tides, and channel geometry is critical for informed management of fluvial resources, especially for transient systems adapting to climate change or human development.

The link between spatial gradients in bed stress (or velocity) and morphological changes in tidal rivers and estuaries is well established. For example, during the development of the Federal Navigation Channel (FNC) in the Columbia River, local expansions in river width were acknowledged to decrease water velocity (and bed stress) and create shoaling hotspots that were then managed by artificially constricting river width with pile dikes and man-made islands (Hickson 1930, 1961). Likewise, Friedrichs (1995) examined 26 systems and established that the cross-sectional area of a tidal channel increases or decreases to minimize along-channel gradients in bed stress. In theory, bed aggradation will occur in the lower reaches of convergent tidal rivers until an equilibrium depth profile is achieved that eliminates spatial gradients in sediment transport (Guo et al. 2014; Bolla Pittaluga et al. 2015). But bed aggradation can also lead to more cataclysmic morphological changes in rivers by producing zones that have an increased likelihood of channel avulsions during flood events (Nittrouer et al. 2012; Chatanantavet et al. 2012). Adjustment of some reaches may be limited by hard-rock features such that they remain out of equilibrium.

Morphological changes are influenced by the interaction of fluvial, tidal, and baroclinic transport processes, which can trap sediment in many ways. Density-driven estuarine circulation can create an estuary turbidity maximum (ETM) near the upstream limit of salinity intrusion, which results from convergent near-bed transport of fine sediments (Festa and Hansen 1978; Talke et al. 2009a), and cause local peaks in channel shoaling (Meade 1969). Landward sediment transport and particle trapping are also generated by settling and scour lag (Chernetsky et al. 2010; Friedrichs et al. 1998; Postma 1961), tidal asymmetry in current magnitudes and durations (Allen et al. 1980; Hoitink et al. 2003; Speer and Aubrey 1985), spatial gradients in vertical mixing due to salinity stratification (Geyer 1993), and correlations of velocity shear and vertical mixing (Jay and Musiak 1994; Jay et al. 2007; 2015; Burchard and Baumert 1998; Burchard et al. 2018). Collectively, exchange flows that are influenced by variations in eddy viscosity are now termed Eddy-Viscosity Shear Covariance (ESCO; Dijkstra et al. 2017) and are known to influence sediment trapping (Jay and Musiak 1994; Burchard et al. 2018). Changes to estuarine circulation and tidal asymmetries induced by channel modification may increase sedimentation in estuaries (Chant et al. 2011; Sherwood et al. 1990) and even lead to hyperturbid and/or hypoxic conditions (Chernetsky et al. 2010; Talke et al. 2009a, b).

Analytical models of tidal sediment trapping and ETM formation usually focus on fine suspended sediments and assume morphodynamic equilibrium, i.e., that erosion equals deposition (Friedrichs et al. 1998, Huijts et al. 2006, Talke et al. 2009b, Dijkstra et al. 2019), so that the models are valid only for small departures from equilibrium. In addition, bed stress, which is typically proportional to a power of the velocity, is often linearized to be proportional to the near-bed velocity (e.g., Chernetsky et al. 2010). Thus, the non-linear interactions between river flow and tidal forcing, and their influence on bed stress (see e.g. Godin et al. 1991), are typically not considered in analytical morphodynamic models. Indeed, analytical representations of bed stress variability due to river/tide interaction are rarely attempted (but see Buschmann et al. 2009; Familkhalili et al. 2022); rather, the integrated response of coupled sediment/tidal behavior, which includes sediment settling lag effects, is evaluated (e.g., Chernetsky et al. 2010). In this contribution, we develop an analytical expression for the along-channel variability in bed stress, which explicitly details the non-linear interactions between river flow and tidal forcing, to better understand how frictional non-linearities influence sediment trapping.

Frictional river/tide interactions can influence the spatial variability in bed stress and produce local minima in bed stress, which are thought to be hotspots of sediment trapping, particularly of the coarser fraction of sand, which is less influenced by water-column settling lag effects (Jay et al. 1990). Transport of sand, whether as bed load or suspended load, is a primary mode of sediment transport in energetic, sand bedded river estuaries (see Templeton and Jay 2012), and is directly related to velocity and bed stress through the Shields parameter (Dyer 1995). However, since most studies of sediment transport in estuaries focus on fine sands, cohesive sediments, and the formation of ETMs from suspended sediment, the possibility that bed stress minima might influence deposition of the coarser sand fraction is much less studied (but see Dalrymple et al. 1992).

Background

Following standard practice, we define bed stress τ_b in terms of the near-bed fluid velocity u_b, fluid density ρ, and a drag coefficient representing the roughness of the bed C_d (Proudman 1952):

$$\tau_b \equiv \rho C_d u_b |u_b|, \tag{1}$$

where the absolute value accounts for the reversal in stress direction that occurs when tidal velocities change sign. If τ_b exceeds a critical threshold, τ_c, sediment is considered to mobilize off the bed. Sediment transport then scales non-linearly with τ_b (Dyer 1986). Because both the fluid velocity and bed roughness vary in space and time (Branch et al. 2021), gradients in bed stress develop that influence erosion and deposition patterns.

In a tidal river, the cross-sectionally averaged bottom velocity u_b is driven by the hydraulic gradients set up by precipitation/watershed runoff and ocean tides, which are referenced herein as the riverine (residual) velocity (U_R) and tidal velocity (U_T). In a 1-D framework (cross-sectionally averaged), assuming a single tidal constituent with no reflected wave, the near-bed velocity at a given location x can be described as follows:

$$u_b = U_T cos\left(\frac{2\pi t}{T} - \phi\right) + U_R, \tag{2}$$

where $U_T(x)$ is tidal velocity amplitude, T is the tidal period, $\varphi(x)$ is tidal phase, $U_R(x) \equiv Q_R/hb$ is the residual (non-tidal) velocity, $h(x)$ is the tidally averaged river depth, $b(x)$ is river width, and $Q_R < 0$ is river discharge. $x = 0$ at the ocean and $x = L$ at the head of tides where $U_T \sim 0$. In the absence of tributary input, Q_R is constant in space. Therefore, convergent channels in which the cross-sectional area decreases monotonically in the upstream direction exhibit river velocities that increase in the upstream direction (Fig. 1). Tidal velocity, by contrast, is forced at the ocean boundary and typically decreases in the upstream direction due to frictional damping. Strong cross-sectional convergence can locally amplify tidal velocity as the wave propagates upstream, but the general trend is for $U_T(x)$ to decrease in the upstream direction in systems with strong river discharge. The result of these two opposing gradients is a local minimum in u_b, and more importantly in τ_b, that leads to convergent sediment fluxes and that may control the morphological character of an alluvial system (Dalrymple et al. 1992).

While a bed stress minimum (and preferential deposition zone) is believed to be common in tidal rivers, the literature is limited on analytical characterizations of its location. Nittrouer et al. (2012) showed that the cross-sectional area of the Mississippi River increases in the downstream direction during low/moderate river discharge, which causes a local minimum in velocity (or bed stress) near the mouth of the river with sediment deposition occurring upstream thereof. Their analysis, however, neglects the influence of tidal velocity on the bed stress and is thus restricted to systems with minimal tidal input, as is appropriate for the micro-tidal environment of the Mississippi. Evaluation of meso- and macro-tidal systems requires consideration of the coupled interaction between the tidal and fluvial velocity fields (Hoitink and Jay 2016).

Giese and Jay (1989), Jay et al. (1990), and Jay et al. (2016) evaluated the energy balance in the Lower Columbia River Estuary (LCRE) demonstrating that, because of tidal damping and channel geometry, tidal and fluvial dissipation are monotonically decreasing/increasing functions from the mouth of the river. As a result, the total dissipation, or bed stress, reaches a minimum at some location upstream of the mouth, x_{min} (Fig. 1). In the LCRE, this local minimum occurs within a locus of sand deposition that extends from roughly river kilometer (*Rkm*) 30 to 56 and that requires anomalously high-dredging quantities to maintain authorized depths in the FNC. The estuary turbidity maximum is also often found in the downstream end of this reach. The evaluation of Giese and Jay (1989) implies that an increase in fluvial dissipation during high river discharge events would shift x_{min} seaward, but a detailed evaluation of the bed stress minimum location was beyond the scope of their analysis.

The ability to evaluate the factors that influence x_{min} is particularly important in the LCRE because, like other systems, the river has been extensively modified since the nineteenth century. The authorized depth of the Lower Columbia River FNC has more than doubled from 6 to 13 m over the twentieth century (Helaire et al. 2019). At the same time, flow regulation has reduced peak flows, and the mean river discharge during the spring freshet (May–July) has decreased from 13,610 m^3 s^{-1} before 1900 to 7060 m^3 s^{-1} between 1970 and 2004 (Naik and Jay 2011). Both channel deepening and flow regulation decrease fluvial dissipation in the system; however, the influence of these activities on x_{min}, and the locus of sand deposition, remains unclear.

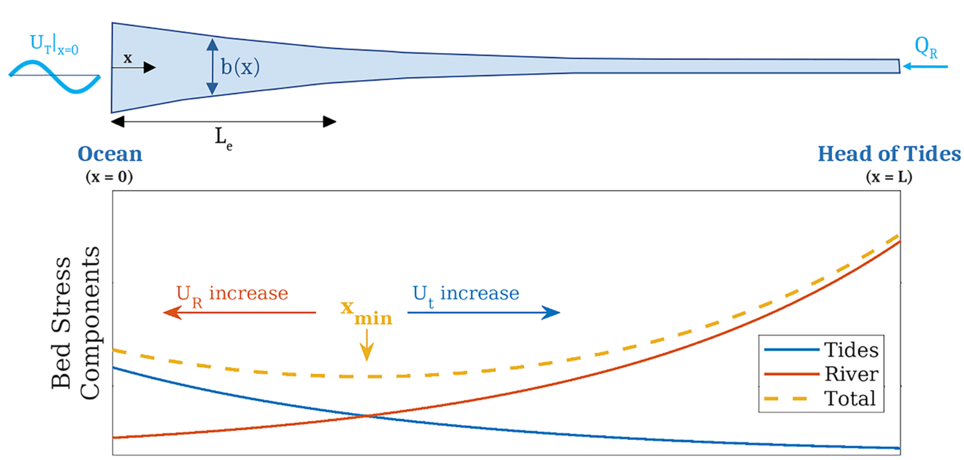

Fig. 1 Plan view of idealized convergent river (top) and resulting along-channel profile of bed stress (bottom)

To test the hypothesis of Giese and Jay (1989) and Jay et al. (2016), we explore the sensitivity of x_{min} to channel geometry and river discharge by adapting the bed stress linearization introduced by Proudman (1952) and later extended by Dronkers (1964). The approach includes spatial variability induced by tidal damping and channel convergence to obtain analytical estimates of x_{min}. Estimates of x_{min} were validated using the 2-D Adaptive Hydraulics (AdH) numerical model using nine convergent channel geometries and six river discharges, a total of 54 simulations. In testing the parameter space, we found that x_{min} is topographically constrained by channel convergence but indeed exhibits variability induced by channel geometry and river discharge as hypothesized above. The theoretical considerations developed herein were applied to three prototype estuaries and show good agreement with their sediment transport characteristics, as described in the literature.

Methods

This section introduces an analytical framework for estimating the location of the bed stress minimum as a function of channel geometry, river discharge, and tidal amplitude. The framework employs a Fourier series decomposition of the non-linear bed stress and the theory of tidal propagation to establish an along-channel profile of the bed stress magnitude $\tau(x)$. This evaluation provides a relatively straightforward approach to examine the spatial distribution of bed stress without the need to solve the equations of motion. The location of the minimum bed stress within the domain, x_{min}, is found using the along-channel derivative of $\tau(x)$ and validated using AdH numerical model simulations.

Fourier Decomposition

Assuming bed velocity is driven by a single tidal constituent and river discharge, the bed stress produces a signal at the fundamental, overtide, and residual frequencies. Following Proudman (1952), the bed stress (Eq. (1)) can be decomposed into contributing frequencies using a Fourier Cosine Series of velocity u_b (Eq. (2)):

$$u_b|u_b| \approx \sum_{n=0}^{\infty} a_n cos\left(\frac{n\pi t}{T}\right), \tag{3}$$

where n represents the individual elements of the series. Because we are interested only in the amplitude of $\tau(x)$, its along-channel phase variability can be neglected. Thus, we use a symmetric cosine series, assuming that phase $\varphi = 0, \pi, 2\pi, \ldots$ in Eq. (2) for all x.

The Fourier coefficients a_n are determined by using the orthogonality of the cosine function (Haberman 2004):

$$a_n = \frac{2}{T}\int_0^T u_b|u_b| cos\left(\frac{n\pi t}{T}\right)dt, \tag{4}$$

and the absolute value is addressed by substituting $u_b.^2$ into the integrand above and recognizing the change in sign induced over the interval [0, T]

$$a_n = \frac{2}{T}\left[2\int_0^{t_1} u_b^2 cos\left(\frac{n\pi t}{T}\right)dt - \int_{t_1}^{t_2} u_b^2 cos\left(\frac{n\pi t}{T}\right)dt\right], \tag{5}$$

where:

$$t_1 = \frac{T}{2\pi}cos^{-1}\left(\frac{-U_R}{U_T}\right) t_2 = T - t_1. \tag{6}$$

Substitution of Eq. (2) into Eq. (5) and evaluating for different values of n gives the magnitude of the bed stress at various frequencies. For a dominantly semidiurnal system, the diurnal tide can be neglected, and the fundamental frequency is given by $n = 2$:

$$\begin{aligned} a_2 = {} & U_T^2\left[\frac{3}{\pi}sin\left(cos^{-1}\left(\frac{-U_R}{U_T}\right)\right) + \frac{1}{3\pi}sin\left(3cos^{-1}\left(\frac{-U_R}{U_T}\right)\right)\right] \\ & + U_R U_T\left[\frac{2}{\pi}sin\left(2cos^{-1}\left(\frac{-U_R}{U_T}\right)\right) + \frac{4}{\pi}cos^{-1}\left(\frac{-U_R}{U_T}\right) - 2\right] \\ & + U_R^2\left[\frac{4}{\pi}sin\left(cos^{-1}\left(\frac{-U_R}{U_T}\right)\right)\right]. \end{aligned} \tag{7}$$

Evaluating Eq. (5) for $n = 0$ gives the bed stress magnitude at residual frequency:

$$\begin{aligned} a_0 = {} & U_T^2\left[\frac{1}{2\pi}sin\left(2cos^{-1}\left(\frac{-U_R}{U_T}\right)\right) + \frac{1}{\pi}cos^{-1}\left(\frac{-U_R}{U_T}\right) - \frac{1}{2}\right] \\ & + U_R U_T\left[\frac{4}{\pi}sin\left(cos^{-1}\left(\frac{-U_R}{U_T}\right)\right)\right] \\ & + U_R^2\left[\frac{2}{\pi}cos^{-1}\left(\frac{-U_R}{U_T}\right) - 1\right]. \end{aligned} \tag{8}$$

We note that both the tidally varying and the residual terms are functions of the tidal velocity squared $U_T{}^2$, the product $U_R U_T$, and the river velocity squared $U_R{}^{2.}$ (cf. Buschman et al. 2009). The remaining Fourier coefficients describe the distribution of the bed stress signal across frequency space, which may manifest at frequencies of other tidal constituents and/or shallow water overtides. When the velocity is composed of a single tidal constituent and river discharge (Eq. (2)), no energy is transferred to odd elements of the series (i.e., $an = 0$ for $n = 1, 3, 5, \ldots$). The non-zero coefficients in Eq. (3) will decrease in magnitude as n increases, and only the first three elements are considered here, i.e., $n = 0, 2, 4$. The first overtide is given by $n = 4$:

$$
\begin{aligned}
a_4 = U_T^2 & \left[\frac{1}{\pi} sin\left(2cos^{-1}\left(\frac{-U_R}{U_T}\right)\right) + \frac{1}{\pi} cos^{-1}\left(\frac{-U_R}{U_T}\right)\right. \\
& \left. + \frac{1}{4\pi} sin\left(4cos^{-1}\left(\frac{-U_R}{U_T}\right)\right) - \frac{1}{2}\right] \\
& + U_R U_T \left[\frac{4}{\pi} sin\left(cos^{-1}\left(\frac{-U_R}{U_T}\right)\right)\right. \\
& \left. + \frac{4}{3\pi} sin\left(3cos^{-1}\left(\frac{-U_R}{U_T}\right)\right)\right] \\
& + U_R^2 \left[\frac{2}{\pi} sin\left(2cos^{-1}\left(\frac{-U_R}{U_T}\right)\right)\right].
\end{aligned} \tag{9}
$$

While the overtide M_6 ($n = 6$) is important in systems with small mean flows, its importance relative to M_4 ($n = 4$) recedes quickly as river flow increases in amplitude from zero. Thus, the M6 term can be safely ignored in the systems considered here.

Equations (7) to (9) are challenging to interpret but can be simplified by noting that when $U_R/U_T = 0$ and 1, respectively, $\cos^{-1}(U_R/U_T) = \pi/2$ and 0, which allows Eq. (7) to be approximated as follows:

$$a_2 \approx \frac{8}{3\pi} U_T^2 + \frac{4}{\pi} U_R^2 \quad 0 \leqslant |U_R| < |U_T| \tag{10}$$

$$a_2 \approx -2U_R U_T \quad |U_R| \geqslant |U_T|. \tag{11}$$

Equations (10) and (11) state that when there is no river discharge, the bed stress magnitude at the fundamental frequency is equal to $8/3\pi(U_T)^2$, which is the classical value cited in the literature (Dronkers 1964; Proudman 1952). The bed stress increases quadratically with U_R for $|U_R| < |U_T|$ and approximately linearly with $|U_R|$ when $|U_R| \geq |U_T|$ (Fig. 2). Note that the error in each approximation grows as U_R/U_T deviates from their respective intervals (Fig. 2).

The coefficient a_0 can be simplified to:

$$a_0 \approx \frac{4U_R U_T}{\pi} \quad 0 \leq |U_R| < |U_T| \tag{12}$$

$$a_0 \approx -\left(\frac{U_T^2}{2} + U_R^2\right) \quad |U_R| \geqslant |U_T|. \tag{13}$$

In contrast to the tidal frequency bed stress, Eqs. (12) and (13) indicate that a_0 is linear in U_R at low river velocities and quadratic at higher velocities (Fig. 2). When tides are absent, the zero frequency bed stress is simply the square of the river velocity (but opposite in sign).

Equation (9) can be approximated as:

$$a_4 \approx \frac{2.4U_R U_T}{\pi} \quad 0 \leq |U_R| < |U_T| \tag{14}$$

$$a_4 \approx \frac{-U_T^2}{2} \quad |U_R| \geqslant |U_T|. \tag{15}$$

Thus, a_4 is approximately proportional to the tidal amplitude U_T and increases approximately linearly with U_R at low river discharge. However, once the river velocity exceeds the tidal velocity, a_4 is no longer a function of U_R (Fig. 3). Because a_4 approaches a constant value while a_2 continues to grow as river velocity increases, there is a U_R/U_T value for which a_4/a_2 is maximum. Plotting Eqs. (7) and (9) reveals this ratio is maximum when $U_R/U_T \approx -0.6$ (Fig. 3b). Note that a_4 is negative because it represents the transfer of energy to the first overtide from the interaction between the fundamental frequency and river discharge.

Equation (14) highlights the requirement for a non-zero river flow (or other tidally averaged flow) for a frictional overtide to be produced, which is not true for all overtide modes (i.e., when $U_R = 0$, $a_4 = 0$ but $a_6 \neq 0$). Also, a_4 is limited by the tidal velocity scale U_T because it is bound from above by U_T^2, such that a_4 is always less than a_2, reaching up to about one-third of the fundamental frequency (Fig. 3b). Because a_4 is generally much smaller than a_2, the overtide mode is not included in subsequent development of the bed stress minimum location. However, overtides are developed in the numerical model discussed below, and the consequences of neglecting a_4 are explored by comparing analytical and numerical model results.

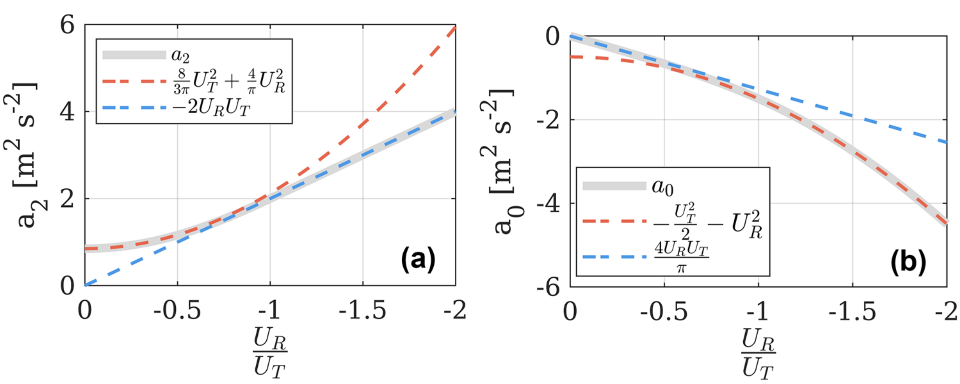

Fig. 2 Tidal frequency bed stress a_2 (**a**) and zero frequency bed stress a_0 (**b**) as a function of U_R/U_T. Equations (7) and (8) are shown by gray solid line; approximations are shown in dashed lines

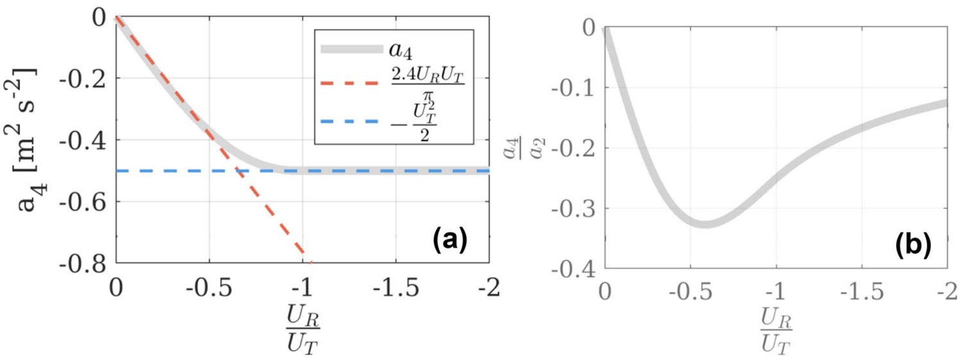

Fig. 3 First overtide frequency bed stress a_4 as a function of U_R/U_T (**a**) with Eq. (9) shown by gray solid line and approximations shown in dashed lines. Ratio of a_4/a_2 as a function of U_R/U_T using Eqs. (7) and (9) (**b**)

The approximations defined in Eqs. (10)–(15) can also be derived using Chebyshev polynomials (see Chapter 8, Sect. 8 in Dronkers 1964), but the cosine series has simpler basis functions, which improves the clarity of exposition. Approximating the bed stress with Chebyshev polynomials is especially useful when deriving analytical solutions to the shallow water equations, because the bed stress can be accurately represented by two or three terms (Godin 1991). A Fourier cosine series, on the other hand, explicitly renders the amplitude of the bed stress at each frequency, which facilitates interpretation of how the bed stress responds to changes in channel geometry and boundary conditions. The Chebyshev polynomials require an extra step using trigonometric identities to decompose the non-linear terms into the tide/overtide modes (Godin 1991). Because we are interested in studying the spectral signature of the bed stress throughout the domain, not solving the equations of motion, a Fourier cosine series is used herein. Fourier's theorem guarantees convergence of the cosine series (Haberman 2004), and the cosine series also avoids the need to change variables associated in defining the Chebyshev polynomials. Finally, in situ observations and numerical modeling of tides are conventionally analyzed using harmonic functions, and so the elements of a Fourier cosine series are more readily compared to results from these other tools.

Bed Stress Minimum Location

The bed stress varies in time due to seasonal fluctuations in river discharge and because U_T and U_R are opposed during flood but in the same direction on ebb. Tidal velocities also vary on daily, monthly, and annual time scales. For our analysis, we focus on spatial variations in peak ebb bed stress magnitude because in a system with substantial river flow such as the Columbia River, the largest stress–and therefore sediment transport–typically occurs during ebb, at least in the parts of the system without salinity intrusion. The interaction of semidiurnal and diurnal tides, which also creates an ebb asymmetry in tidal currents on the US West Coast (see Nidzieko 2010), will be considered in a future analysis. Below, we investigate the conditions required for this assumption to be valid. Subtracting Eq. (10) from Eq. (13) gives

$$\left|\tau_{ebb}\right| = a_0 - a_2 \approx \frac{-4}{\pi}U_T^2 - \frac{7}{\pi}U_R^2. \tag{16}$$

Equation (16) captures the magnitude of bed stress during peak ebb, which occurs at different times along the ocean-river continuum. This approach allows evaluation of neap-spring and seasonal variations in bed stress. In rivers wherein the largest bed stress occurs during flood, the bed stress minimum location may be examined using along-channel profiles of peak flood bed stress by adding Eqs. (10) and (13) (rather than subtracting).

Using Eqs. (10) and (13) limits the applicability of Eq. (16) to regions where $U_R/U_T < 1$. Outside of this range, the tidal frequency bed stress is overestimated by Eq. (10) (Fig. 2). Note, however, that along-channel profiles of bed stress estimated using $(-4/\pi\ U_T^2 - 7/\pi\ U_R^2)$ and $(a_0 - a_2)$ were found to be consistent in the vicinity of the bed stress minimum, and so this limitation does not practically constrain the utility of using the simpler approximation when deriving an expression for x_{min}.

The along-channel variability of $|\tau_{ebb}|$ is evaluated by developing functional forms for U_T and U_R. The domain of interest extends from the ocean ($x = 0$) to the head of tides ($x = L$), where $U_T(L) = 0$ (Fig. 1). Following Jay (1991), U_T is defined using the shallow water equation by assuming a spatially constant tidally averaged river depth $h(x) = H$ and convergent width, $b(x) \sim e^{\gamma x}$. While real systems have local variations in depth and width, this simple representation approximates the geometry of many coastal plain estuaries, allows an analytical solution of the tidal velocity throughout the domain, and is a common approach used in the literature when studying tidal propagation in estuaries (Ianiello 1979; Lanzoni and Seminara 2002; Savenije 2005; Talke and Jay 2020). This approach assumes that the tidal amplitude is small relative to H, the flow is unstratified (though non-zero salinity and a weak mean salinity gradient may be present in the domain), and the spatial acceleration term is negligible.

In an estuary with moderate topography and no reflected wave, the tidal amplitude takes the form of an exponential function (Jay 1991):

$$U_T \approx U_{T0} e^{\left(p-\frac{\gamma}{2}\right)x}, \tag{17}$$

where U_{T0} is the tidal amplitude at the mouth, $p < 0$ is the damping modulus, and γ scales the width convergence ($b(x) \sim e^{\gamma x}$) and is defined using an e-folding length scale Le ($\gamma = -1/Le < 0$). When friction is stronger than topographic funneling ($|p| > |\gamma/2|$), the tidal velocity decays exponentially from the mouth. The use of an approximate tidal velocity (Eq. 17) to estimate the location of the bed stress minimum is validated through comparison with AdH Model results (see next section).

The river velocity U_R is defined by the river discharge divided by the channel cross-section. Assuming an exponentially convergent width ($b(x) = B_0 e^{\gamma x} + B_1$) gives

$$U_R = \frac{Q_R}{\left(B_0 e^{\gamma x} + B_1\right)H}, \tag{18}$$

where B_0 is river width at the mouth and B_1 is river width as $x \to \infty$.

Substituting Eqs. (17) and (18) into Eq. (16), and evaluating when the x-derivative equals zero, provides an implicit solution for x_{min}:

$$\frac{x_{min}}{L_e} = -ln\left[\left(\frac{7}{4}\left(\frac{Q_R}{HB_0U_{T0}}\right)^2\left(\frac{p}{\gamma}-\frac{1}{2}\right)^{-1} e^{(2\gamma-2p)x_{min}}\right)^{1/3} - \frac{B_1}{B_0}\right]. \tag{19}$$

Finally, developing an explicit equation facilitates interpretation of the sensitivity of x_{min}. Assuming a range of typical values for p [$-5(10^{-5})$, $-1(10^{-6})$ m^{-1}], γ [$-5(10^{-5})$, $-1(10^{-5})$ m^{-1}] and x [0, 100 km], the average of $e^{(2\gamma-2p)x/3}$ equals one, and the standard deviation is 0.26 (see Fig. S1 in supplement). And so x_{min} can be approximated by assuming $e^{(2\gamma-2p)x/3}$ is equal to one:

$$\frac{x_{min}}{L_e} = -ln\left[\left(\frac{7}{4}\left(\frac{Q_R}{HB_0U_{T0}}\right)^2\left(\frac{p}{\gamma}-\frac{1}{2}\right)^{-1}\right)^{1/3} - \frac{B_1}{B_0}\right]. \tag{20}$$

Note that $e^{(2\gamma-2p)x/3}$ equals one when $p = \gamma$. When $p/\gamma < 1$, Eq. (20) underestimates Eq. (19), while weaker convergence relative to damping $p/\gamma > 1$ leads to overestimates by Eq. (20) (see Fig. S2 in supplement).

AdH Model

Equation (20) was validated using the 2-dimensional, vertically integrated module of the AdH numerical model (Savant et al. (2011); see also https://hdl.handle.net/11681/39080). The domain, which extended 200 km landward from the ocean boundary, was defined as an exponentially convergent channel that relaxes to a constant width far upstream: ($b = 4{,}000e^{\gamma x} + 800\ m$) (see Fig. 1). Bed elevation was constant throughout the domain, and the grid contained anywhere between 1500 and 3000 elements, depending on γ. The channel geometry was chosen to produce a large range in x_{min} values when using the inputs from Table 1 in Eq. (20). The model was forced by the M_2 tide at the mouth with an amplitude of 0.8 m and constant river discharge at the upstream boundary. Simulations were run for 2 weeks using a maximum time step of 300 s. Trials were carried out under three different convergence length scales, three river depths, and six river discharges, yielding 54 individual runs (Table 1).

In order to define the bed stress minimum location for each trial (x_{adh}), time series of velocity at each node were extracted from the AdH model output to define the bed stress throughout the domain as $\tau = \rho\ Cd\ U\ |U|$, where ρ is water density, C_d is a drag coefficient, and U is the cross-sectionally averaged along-channel velocity (ebb velocity negative). The drag coefficient within a real system can vary between roughly 0.001 and 0.01 (Branch et al. 2021) and was assumed to equal 0.0026, following prior studies in tidal rivers (Giese and Jay 1989; Friedrichs and Aubrey 1994; Ralston et al. 2019). Along-channel profiles of the bed stress were then plotted at each time step to define an envelope of bed stress along the river that illustrate the maximum, minimum, and range of bed stress at each location during the tidal cycle (see, for example, the gray shading in Fig. 4). For each trial, the location of the x_{adh} was defined as the location where the bed stress envelope shows a local minimum during ebb (red squares in Fig. 4). Of the 54 simulations, 30 exhibited a bed stress minimum within the domain. For these trials, x_{min} was defined by substituting the boundary conditions and geometry of the AdH model into Eq. (20). The damping modulus p and U_{T0} were estimated by harmonic analysis of the AdH-derived velocity field.

This study focuses on spatial patterns of bed stress, the location of the bed stress minimum in particular, to infer general trends in sediment transport. Other measures that are traditionally considered for evaluating long-term erosion and deposition patterns are flow predominance and net sediment transport. These two criteria were assessed

Table 1 River discharge, depth, and convergence length scenarios used in AdH runs

River discharge, Q_R [m^3s^{-1}]	–{2000, 4000, 6000, 10000, 14000, 18000}
River depth, H [m]	{6, 9, 12}
E-folding length, L_e [km]	{40, 80, 120}

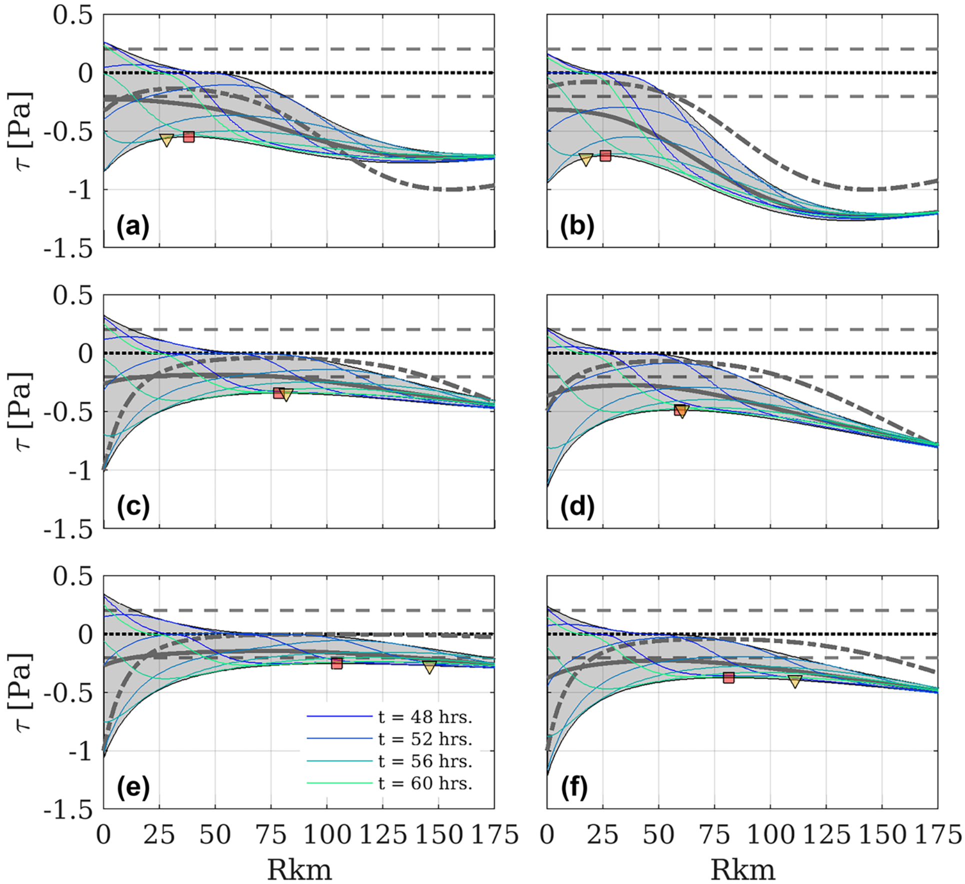

Fig. 4 Along-channel profile of bed stress computed in AdH models when river discharge equals 4000 m^3s^{-1} (left) and 6000 m^3s^{-1} (right) and e-folding length scale equals 40 Rkm (top), 80 Rkm (middle), and 120 Rkm (bottom). Tidally averaged bed stress shown by solid line. Excess bed stress τ_E, normalized by its maximum value in the domain, is shown by dash-dotted lines. Dashed lines represent critical shear stress for fine sand $D_{50} = 0.25$ mm, defined using Shields Diagram. Dotted line shows zero bed stress. Red square marks x_{adh}. Yellow triangle marks x_{min}

using AdH model simulations to highlight the influence of the bed stress minimum on sediment transport. Flow predominance was defined using tidally averaged bed stress profiles and AdH derived bed stress envelopes (as defined below). Excess bed stress ($|\tau_b|$-τ_c) is commonly used to estimate sediment transport (see Dyer 1995), and the sum of this value squared during the AdH model simulation τ_E was used as a proxy for net sediment transport:

$$\tau_E = \int_t sign(\tau_b)\left(|\tau_b| - \tau_c\right)^2, \tag{21}$$

where the *sign()* is needed to maintain direction of transport as τ_b changes sign, and only τ_b values greater than τ_c are included in the integration. Unless otherwise noted, τ_c is assumed to be 0.2 N m^{-2}. This uses Shields criterion (Dyer 1995): $\tau_c = 0.05(\rho_s\text{-}\rho)gD_{50}$, where $\rho_s = 2650$ kg m^{-3} is the particle density, $D_{50} = 0.2\ mm$ is particle diameter, and g is the acceleration of gravity.

Results

This section outlines comparisons between analytical estimates of the bed stress minimum location (Eq. (20)) and AdH model simulations. The sensitivity of x_{min} to channel geometry, tidal amplitude, and river discharge is then explored by studying the properties of Eq. (20).

AdH Model and Validation

AdH-derived bed stress envelopes highlight the connection between the bed stress minimum location and the transition from tidally to fluvially dominated dynamics in the river. As tidal velocities decrease in the upstream direction due to friction, the range of bed stress over a tidal cycle is also smaller (Fig. 4). The proportion of time during the tidal cycle when the bed stress is greater than zero (flood tide) also becomes smaller, tending towards zero somewhere near the bed stress minimum. Because river velocity is largest in the narrow, upstream part of the model domain, the most negative, tidally averaged bed stress typically occurs at the upstream boundary (solid gray line in Fig. 4). Moving downstream, increases in channel width decrease the river velocity and the fluvial contribution to the bed stress (Figs. 5 and 6). A local minimum in modeled bed stress, x_{adh}, manifests where the tidal contribution begins to balance the downstream decrease in U_R. While x_{adh} sometimes occurred in the region where 1/3 <| UR/UT |< 14, over half of the trials exhibited bed stress minima within the tidal-fluvial transition wherein 1 <| UR/UT |< 3. As width convergence and discharge increased, the tidal-fluvial transition and x_{adh} were found to move downstream.

Although the velocity acts primarily at residual and tidal frequencies, the overtide mode also contributes to U in the AdH simulations (solid lines in Fig. 5). The overtide contribution reaches a maximum between the mouth and x_{adh}, reaching about 15% of the total velocity. While the relative phase difference between U2 and U4 ($2\varphi_2 - \varphi_4$) indicates that the tidal velocity is slightly flood dominant throughout the domain ($0 < 2\varphi_2 - \varphi_4 < \pi/2$), the total velocity is ebb dominant because U_R is greater than U_4.

The overtide mode also contributes to AdH-derived bed stress, but in this case, the relative phase difference between a_2 and a_4 ($2\theta_2 - \theta_4$) transitions from ebb dominant near the mouth ($2\theta_2 - \theta_4 \approx \pi$) to slightly flood dominant near and upstream of x_{adh} (Fig. 6). Again a_0 is greater than a_4, and so the total bed stress is ebb dominant. Because Eq. (16) does not include a_4, analytical estimates of τ_{ebb} will overestimate AdH ebb tide bed stress in regions where the bed stress is flood dominant and underestimate AdH in ebb-dominant regions (see dashed vs solid lines in Fig. 6). The difference between τ_{ebb} and AdH ebb tide bed stress was typically small and did not exceed 0.05 m^2s^{-2} at any given location.

Analytical estimates of the residual and tidal bed stress components (Eqs. (7)–(8)) agree well with harmonic analysis of AdH bed stress (within 0.02 m^2s^{-2}; Fig. 6). Small discrepancies are evident near where along-channel profiles of |U4| reach a maximum (see Figs. 5 and 6), likely because U4 is not included in Eq. (2). Analytical estimates of the overtide frequency bed stress (Eq. (9)) generally do not agree with AdH estimates because Eq. (9) represents the bed stress produced by the interaction of UR and UT alone, whereas AdH also includes the contribution of U4. Errors between Eq. (9) and AdH reach about 0.05 m^2s^{-2}, but the greatest difference between the two approaches is that Eq. (9) does not produce the shift from ebb to flood dominance that is evident in the AdH model. Further study of the overtide frequency bed stress must, therefore, include the U4 contribution to the velocity field when calculating the Fourier coefficients for U|U|.

Despite the discrepancies noted above, comparisons between x_{adh} and x_{min} (Eq. (20)) show that, even when omitting the first overtide in Eq. (2), the analytical results are qualitatively consistent with numerical results. Estimates of x_{adh} and x_{min} were found to be well correlated ($R^2 = 0.8$ and p-value ≈ 0) and to share a linear relationship that follows a 1:1 slope (see Fig. 7). Equation (20) is biased above x_{adh} during low flows when $Le = 120$ km (Fig. 4), however, which

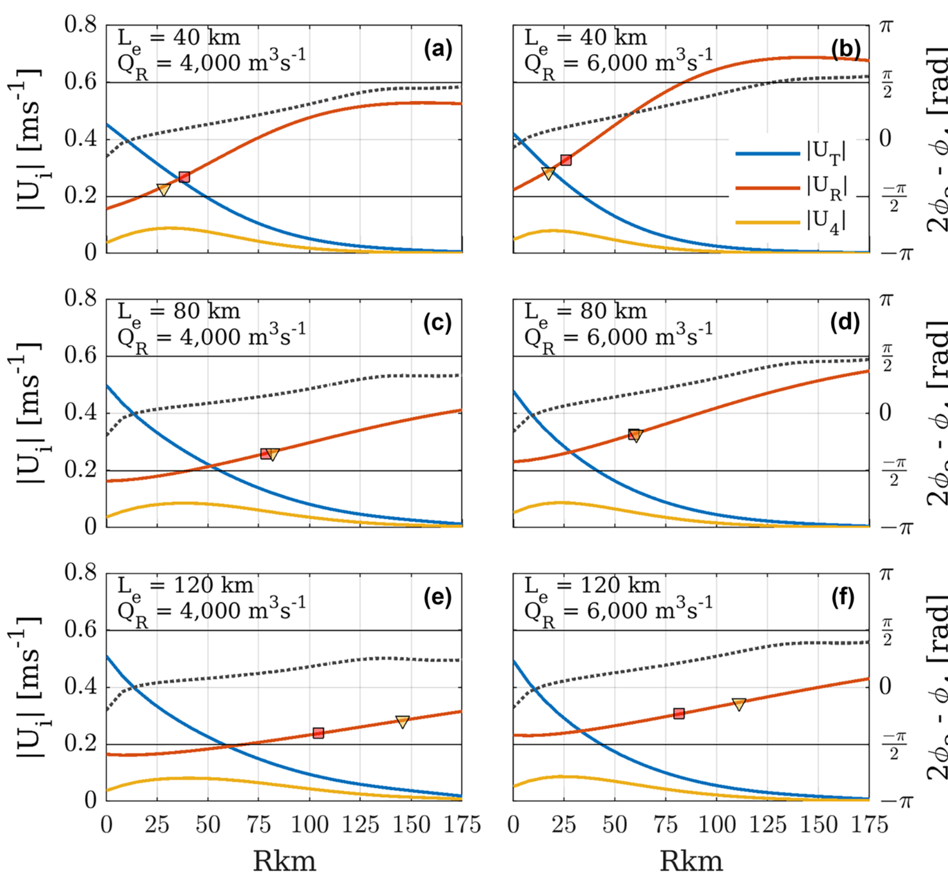

Fig. 5 Along-channel profile of velocity at residual (solid red lines), tidal (solid blue lines), and overtide (solid yellow lines) frequency computed using harmonic analysis of AdH modeled velocity. Results are shown for river discharge of 4000 m^3s^{-1} (left) and 6000 m^3s^{-1} (right) and e-folding length scales of 40 Rkm (top), 80 Rkm (middle), and 120 Rkm (bottom). Phase difference between U_T and U_4 ($2\varphi_2 - \varphi_4$) is shown by a gray-dotted line and indicates that the tidal velocity is flood dominant. Red squares denote x_{adh} and yellow triangles x_{min}

Fig. 6 Along-channel profiles of Fourier coefficients (a proxy for bed stress) for river discharge of 4000 m^3s^{-1} (left) and 6000 m^3s^{-1} (right) and e-folding length scales of 40 Rkm (top), 80 Rkm (middle), and 120 Rkm (bottom). Coefficients are shown at residual (red lines), tidal (blue lines), and overtide (yellow lines) frequency. Analytical estimates (Eqs. (7)–(9)) are shown by dashed lines. Harmonic analysis of AdH modeled bed stress ($U|U|$) is sown by solid lines. Total bed stress during ebb in AdH simulation (solid) and Eq. (16) (dashed) are shown by green lines. The relative phase differences between a_2 and a_4 are shown as dotted lines. Red squares denote x_{adh}

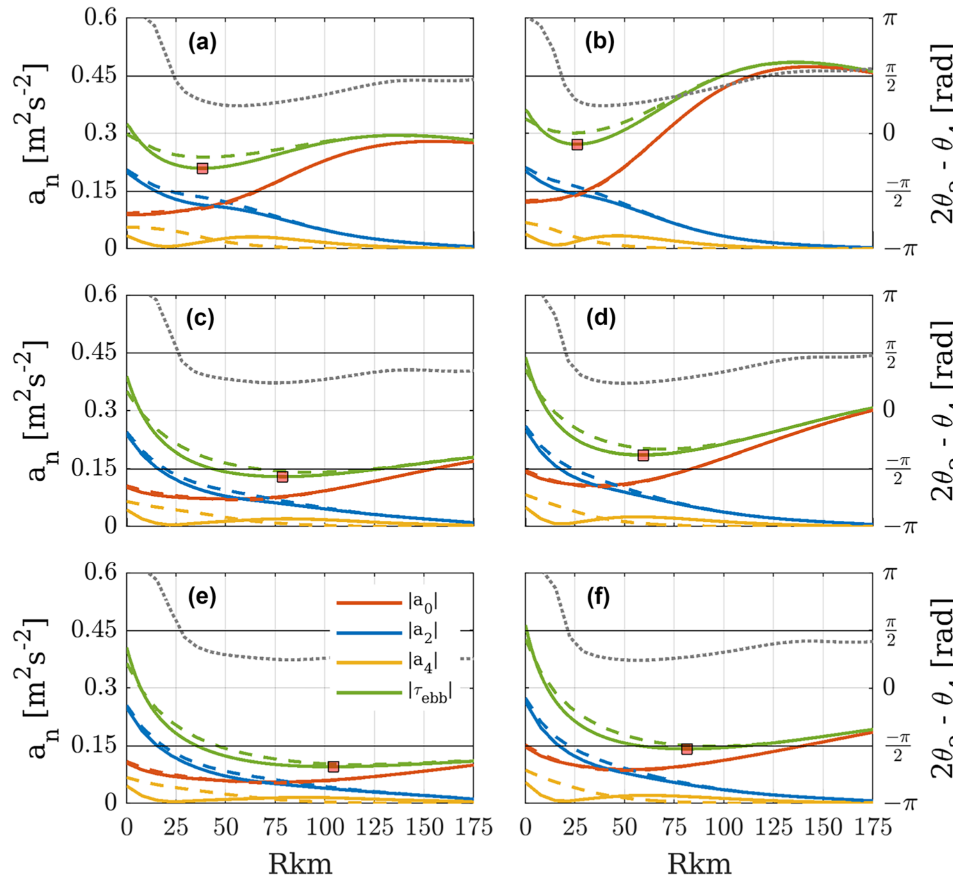

can be attributed to the lack of an overtide mode in the analytical formulation. These trials also had p/γ ratios close to three, which can lead to overestimates of the bed stress minimum location using Eq. (20) (see Fig. S2 in Supplement). The ~70-km discrepancies observed in these trials correspond to a bed stress envelope with small along-channel

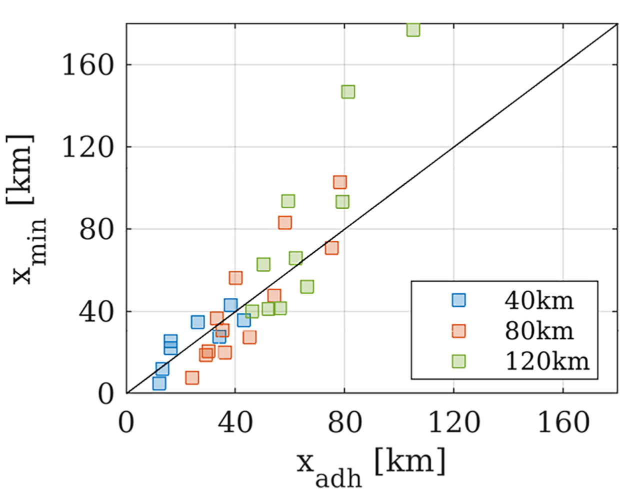

Fig. 7 Location of bed stress minimum in Eq. (20) vs x_{adh}. Solid line depicts a 1:1 slope

gradients in the upper reaches of the river where the bed stress minimum was located (e.g., Fig. 4f). Under such conditions, the bed stress minimum is better described as a ~50-km region rather than a discrete location of reduced bed stress, in which case the discrepancies in Fig. 7 are less significant. Also, x_{min} shows greatest sensitivity to small changes in boundary conditions and geometry when the bed stress minimum is upstream of *Le* (see Fig. 8), which may also contribute to the bias observed for these trials.

Excess bed stress (Eq. (21)) is largest at the upstream boundary for strongly convergent geometries and at the river mouth for weakly convergent geometries (dash-dotted lines in Fig. 4). In both cases, the along-channel profile of τ_E shows a local minimum somewhere near x_{adh}. Excess bed stress τ_E was found to be negative (ebb-dominant) throughout the model domain, so the gradients in τ_E imply sediment accumulation upstream of x_{adh} (at any given control volume, more sediment enters at the upstream boundary than leaves through the downstream boundary) and sediment loss downstream of x_{adh}. Substituting different values of D_{50} into Eq. (21) changed the magnitude of τ_E throughout the domain, but not the qualitative aspects of its along-channel distribution. τ_E exhibited a local minimum near x_{adh} for both finer and coarser grain sizes. Larger particles resulted in a region of limited particle mobility wherein $\tau_E = 0$, which was centered on x_{adh}.

Fig. 8 x_{min} as a function of Q_R/HB_0U_{T0} (left), p/γ (center), and B_1/B_0 (right)

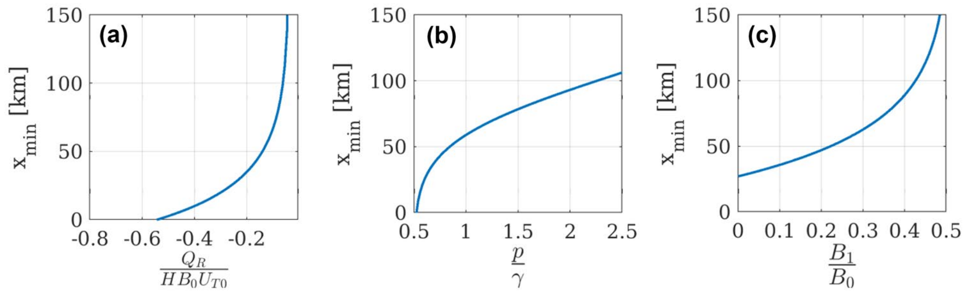

Sensitivity Study

The non-dimensional location of the bed stress minimum x_{min}/L_e is a function of three non-dimensional variables: the ratio of river velocity to tidal velocity at the mouth $Q_R/(HB_0U_{T0})$, the ratio of tidal damping to convergence p/γ, and the ratio of the river widths at the upstream and seaward boundaries B_1/B_0 (Eq. (20)). The sensitivity of x_{min} to these parameters is discussed below. Throughout this section, all parameters in Eq. (20) are assumed to be equal to the values outlined in Table 2 unless otherwise noted.

Because the location of the bed stress minimum is defined through the natural logarithm, x_{min} is most sensitive to changes in boundary conditions and/or geometry when the argument of the natural log function is close to zero or when:

$$\left(\frac{7}{4}\left(\frac{Q_R}{HB_0U_{T0}}\right)^2\left(\frac{p}{\gamma}-\frac{1}{2}\right)^{-1}\right)^{1/3}\approx\frac{B_1}{B_0}. \tag{22}$$

With the parameters used here, this threshold occurs when $|Q_R/(HB_0U_{T0})| = 0.04$, which represents the furthest upstream limit of the applicability of the equations. Values smaller than this yield a complex number from the log function. Values just larger than 0.04 produce the maximum sensitivity of x_{min} to external forcing (Fig. 8a). In other words, the spatial variability of the bed stress minimum is greatest when x_{min} is near the upstream reaches of the domain (e.g., when river discharge is small) and decreases as x_{min} approaches the mouth. A greater sensitivity of x_{min} in the narrowest part of the river is reasonable because small changes in discharge or geometry have greater effect on the river velocity (and hence bed stress) in that location than in wider reaches of the river.

The condition for which x_{min} is exported to the ocean in the analytical model occurs when the argument of the logarithm (see Eq. (20)) is less than or equal to unity:

$$\left(\frac{7}{4}\left(\frac{Q_R}{HB_0U_{T0}}\right)^2\left(\frac{p}{\gamma}-\frac{1}{2}\right)^{-1}\right)^{1/3}-\frac{B_1}{B_0}\leq 1. \tag{23}$$

Under these conditions, $x_{min} \leq 0$, which is outside the validity of the model, and the minimum stress within the domain occurs at $x = 0$. Recall that the analytical model assumes a single-layer (barotropic) flow, and so the bed stress minimum may reside further upstream or require greater river discharge for export when baroclinic circulation dominates velocities near the bed. Solving for Q_R in Eq. (23) provides the river discharge at which the bed stress minimum is exported:

$$Q_{R0}\geq -HB_0U_{T0}\left(\frac{4}{7}\left(\frac{p}{\gamma}-\frac{1}{2}\right)\left(1+\frac{B_1}{B_0}\right)^3\right)^{1/2}. \tag{24}$$

In fact the river discharge required for the bed stress minimum to reside at any location x within the domain is given by:

$$Q_{Rx}=-HB_0U_{T0}\left(\frac{4}{7}\left(\frac{p}{\gamma}-\frac{1}{2}\right)\left(e^{\gamma x}+\frac{B_1}{B_0}\right)^3\right)^{1/2}. \tag{25}$$

For parameter values which resemble the Columbia River (Table 2), Eqs. (24) and (25) indicate that the discharge needs to reach about 7000 m^3s^{-1} or 22,000 m^3s^{-1} for the bed stress minimum to be located at the e-folding length scale or be exported to the ocean, respectively. The former value is slightly less than the modern average flow and about 90% of the historic mean flow (Naik and Jay 2011). The latter value is about equal to the 2-year return flow before 1900, i.e., before system alteration (Jay and Naik 2011). In other words, x_{min} equals about 40 km on average in the LCRE, and the bed stress minimum is exported only during extreme events (see Fig. 11b). Note that for QR = 22,000 m^3 s^{-1}, the LCRE is mostly freshwater, and so the assumption of depth-integrated conditions is justified (Al-bahadily 2020). A minimum bed

Table 2 Assumed values for variables used in sensitivity studies, which are representative of the Lower Columbia River Estuary

River discharge, Q_R [m^3s^{-1}]	−6000
River depth, H [m]	10
River width at ocean boundary, B_0 [m]	4000
River width at upstream boundary, B_1 [m]	800
E-folding length, L_e [km]	40
Tidal amplitude at ocean boundary, U_{T0} [ms^{-1}]	1.0
Damping modulus, p [m^{-1}]	$-2e^{-5}$

stress occurs within the domain when the ratio of river transport to tidal discharge $|Q_R/(HB_0U_{T0})|$ is < 0.54. Thus, $x_{\min}$ is exported when Q_R is more than about half of the tidal discharge. Less convergent systems require a greater Q_R/Q_T ratio to export the bed stress minimum, because x_{min} is typically located further upstream in such systems (Eq. (24); Fig. 8b).

Equation (20) suggests that increasing river velocity, whether by changing river discharge or by decreasing cross-sectional area, tends to move x_{min} downstream. Thus, stronger convergence relative to tidal damping reduces x_{min} (Fig. 8b). Likewise, decreasing B_1 relative to B_0 (narrower upstream cross-sections) reduces x_{min} (Fig. 8c). Physically this represents the relative increase in the fluvial contribution to the bed stress in the upriver reaches when convergence increases, thus translating x_{min} seaward to a location where U_R decreases enough to produce a local minimum. Similarly, shallower systems exhibit bed stress minima that are further seaward relative to deeper systems (Fig. 8a).

The functional form of Eq. (20) highlights that x_{min} is defined as the product between the e-folding length scale and some function of the river geometry and boundary conditions:

$$x_{min} = L_e * f\left(Q_R, U_{T0}, p, \gamma, B_0, B_1, H\right). \quad (26)$$

Therefore, x_{min} is closely related to L_e and will move downstream and exhibit less sensitivity to changing boundary conditions as convergence increases (Fig. 9). Experimentation with different geometries and boundary conditions reveals that the bed stress minimum in large rivers like the LCRE has the greatest likelihood of occurring at or just upstream of the e-folding length scale. For example, when *Le* equals 60 km and all other variables in Eq. (20) are uniformly sampled across the sets defined in Table 3, x_{min} equals 69 km on average with a standard deviation of 80 km. When *Le* equals 120 km, x_{min} equals 180 km on average with a standard deviation of 160 km (Fig. 10). Qualitatively, larger variations of x_{min} in less convergent channels

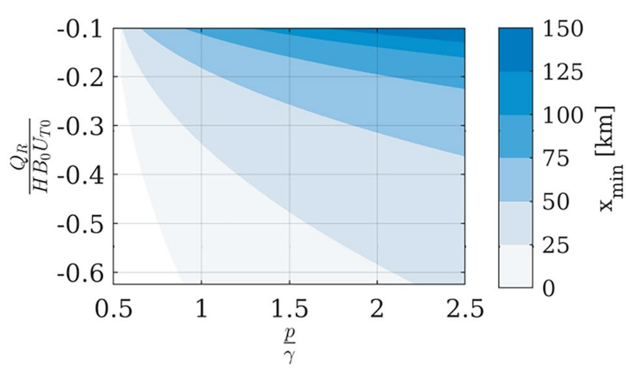

Fig. 9 x_{min} parameter space as function of velocity scale (y-axis) and friction scale (x-axis). Values are produced using variables from Table 2 in Eq. (20)

Table 3 Variable sets sampled for producing x_{min} probability distributions in Fig. 10

River discharge, Q_R $[m^3s^{-1}]$	[−20,000, −1000]
River depth, H $[m]$	[5, 40]
River width at ocean boundary, B_0 $[m]$	[1000, 6000]
River width at upstream boundary, B_1 $[m]$	[400, 1000]
Tidal amplitude at ocean boundary, U_{T0} $[ms^{-1}]$	[0.2, 2]
Damping modulus, p $[m^{-1}]$	[−5e^{-5}, −1.5e^{-5}]

result from a smaller along-channel gradient in river velocity (Fig. 5), wherein changes to boundary conditions cause relatively larger translations in x_{min}. Bed stress minima situated further upstream are also associated with smaller along-channel gradients in tidal velocity, which supplements larger translations in x_{min}. Finally, because the range of x_{min} values moves downstream as L_e decreases, stronger convergence means the bed stress minimum is exported to the ocean (x_{min} < 0) over a greater range of the parameter space (Fig. 10).

Hypersynchronous estuaries lead to a complex number in Eq. (20) because $(p/\gamma - ½)$ is negative. In such systems, the spatial gradients in the tidal and river velocities are not conducive for the formation of a bed stress minimum because both increase in the upstream direction. Some estuaries are hypersynchronous near the mouth, but at some point further upstream, the changes in width become inconsequential, and tidal velocity decreases. Presumably, this puts the bed stress minimum farther upstream. Weakly convergent channels host bed stress minima near the upstream boundary because the river velocity is relatively constant along the channel. When tidal damping is minimal $(p/\gamma \sim ½)$, the bed stress minimum is located near the mouth because the tidal velocity is relatively constant (Fig. 9).

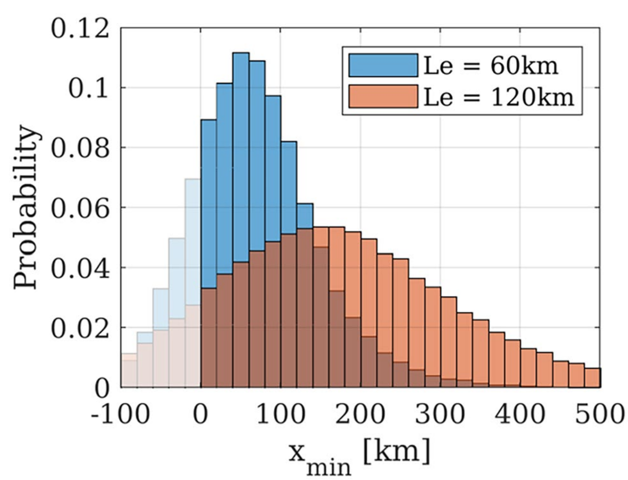

Fig. 10 Probability distribution of x_{min} as estimated by Eq. (20) using variable sets listed in Table 3. x_{min} less than zero indicates that the bed stress minimum has been exported to the ocean, but holds no other physical meaning

Discussion

The dependence of x_{min} on depth and river discharge suggests that any shifts to system morphology and boundary conditions, whether caused naturally or by system management, can result in large shifts in the bed stress minimum and therefore the locations of sediment deposition. Rivers all over the world are being deepened to facilitate passage for ever larger vessels (Talke and Jay 2020), which suggests that the bed stress minimum has migrated upstream in many rivers. In this section, historical changes in bed stress profiles and bed stress minimum locations are explored in three prototype systems (Lower Columbia River Estuary or LCRE, Delaware Estuary, and Hudson River) to illustrate how management over the last century may have influenced sediment transport and deposition near x_{min}. For each system, daily averaged river discharge observations between 2000 and 2020 and idealized geometry (Table 4) are substituted into Eq. (20) to develop probability distributions of x_{min} for modern and historical channel depths. Bed stress profiles are generated using $|\tau_{ebb}| = a_0 - a_2$ (see Methods section).

Lower Columbia River Estuary

Before channel improvements beginning in the late 1870s, controlling depths in the LCRE were about 6–8 m (Hickson 1961; Helaire et al. 2019). While in-water placement of dredged material has maintained shallower depths outside the FNC, the increase in ship-draft over the last 150 years has driven depth increases all along the river. Historical cross-sections before channel improvement show many reaches with an average depth of 7 m or less (Hickson 1961). In contrast, recent bathymetry surveys indicate that the average depth of the LCRE is on the order of 10 m upstream of the estuary (Rkm 50), consistent with the idea that dredging has exceeded sand supply for most years since 1905 (Templeton and Jay 2012). As has happened in other systems where hydropower regulation of flow has reduced flows, sediment supply has decreased (Jay and Simenstad 1996; Naik and Jay 2010, 2011). Agricultural diversion, flood control, reservoir trapping of sediment, and decreased flows due to climate change since the late 1800s have all contributed to decreased sediment input at the same time that dredging has removed large amounts of sand (Naik and Jay 2011).

Substitution of values representative of the LCRE (Table 2) into Eq. (20) along with daily average river discharge measured at Rkm 87 from 2000 to 2020 suggests how the probability distribution of x_{min} may have shifted due to channel deepening. Assuming an average river depth of 7 m before 1900, the average value of x_{min} is 33 km and seasonal variability in river discharge shifts x_{min} by 75 km (Fig. 11b). During low flow, late summer months, x_{min} is near Rkm 75, while it is within a few kilometers of the mouth during flood events. With a deeper river (H = 10 m), the average location for the bed stress minimum shifts upstream by 15 km to Rkm 48, and seasonal patterns in the hydrograph shift x_{min} by roughly 100 km, from Rkm 5 to Rkm 115. Because the parameterization of tidal amplitude does not include the damping effects of river discharge (U_{T0} and p are constant in Table 2), seasonal fluctuations in x_{min} are potentially greater in the LCRE than Eq. (20) suggests.

Channel deepening can influence shoaling volumes upstream of x_{min} through modifications to the along-channel profile of bed stress. For example, a deeper channel exhibits smaller bed stress magnitudes and reduced bed stress gradients upstream of x_{min} than a shallower channel (Fig. 11a). Because the bed stress is uniformly greater than the critical value for particle movement, as defined using Shields Diagram with a mean particle diameter $D50$ = 0.25 mm, sand deposition is controlled by spatial gradients in transport, which suggests that deepening could reduce shoaling upstream of x_{min} even though the bed stress decreases.

Flow regulation on the LCRE has influenced the bed stress minimum through a reduction in peak seasonal flows. For example, the mean river discharge during the spring freshet (May–July) decreased from 13,610 m^3 s^{-1} before 1900 to 7060 m^3 s^{-1} between 1970 and 2004 (Naik and Jay 2010). According to Eq. (20), this decrease in river discharge results in an upstream shift in x_{min} of 25 km during the freshet (from Rkm 15 to Rkm 40). In fact, the bed stress minimum does not occur in the estuary under pre-regulation peak freshet flows (~22,000m^3 s^{-1}), whereas $x_{min} \approx 30$ km during present day peak freshet flows (~9000m^3 s^{-1}). While salinity intrusion limits sand export, salinity was essentially expelled from the Columbia River estuary on greater ebbs during pre-1900 high flows (Sherwood et al. 1990; Al-bahadily 2020). Together with the changes in river depth, flow regulation has created a system that is likely no longer capable of exporting the bed stress minimum (except under very large flood events), which suggests that less material is being supplied to the

Table 4 Idealized representation of example estuaries

Variable	Delaware Estuary[a]	Hudson River Estuary[b,c]
B_0 $[m]$	45,000	1900
B_1 $[m]$	300	200
L_e $[km]$	35	60
U_{T0} $[ms^{-1}]$	0.8	0.7
p $[m^{-1}]$	$-2e^{-5}$	$-1.5e^{-5}$

[a]Pareja-Roman et al. (2020)

[b]Ralston and Geyer (2017)

[c]NOAA tide and current predictions

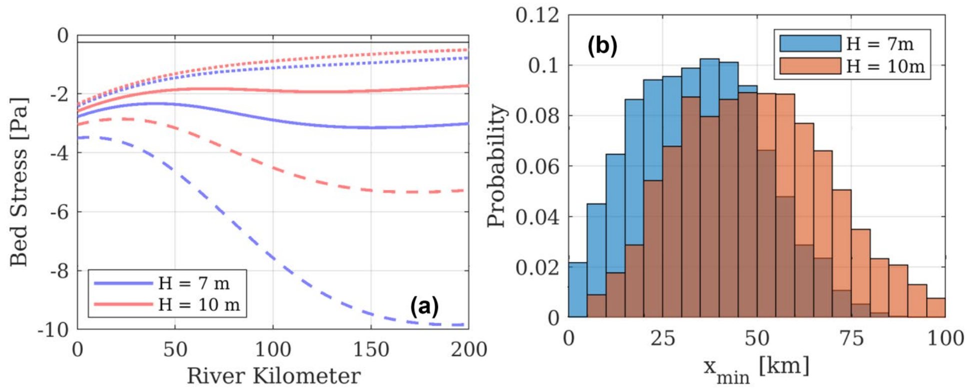

Fig. 11 Left: Bed stress profiles (Eq. (16)) in idealized Columbia River for river discharge of 2000 (dotted lines), 5000 (solid lines), and 10,000 (dashed lines) m^3s^{-1} assuming historical (blue lines) and contemporary channel depths (red lines). Solid black line denotes critical bed stress for movement of medium sand (D_{50} = 0.25 mm). Right: Columbia River x_{min} as calculated using Eq. (20) using river discharge measurements > 2000 m^3s^{-1} collected between 2000 and 2020 at USGS Station 14246900 (~Rkm 86)

Columbia River plume and the Washington coast now than was a century ago. Indeed, shoreline erosion near the mouth of the Columbia River since the 1950s has been attributed to insufficient sediment supply from the estuary (Kaminsky et al. 2010; Elias et al. 2012). According to Eq. (24), river discharge needs to reach about 22,000 m^3 s^{-1} under present-day river depths and 15,000 m^3 s^{-1} when $H = 7$ m before the bed stress minimum is expelled. Daily averaged discharge at Rkm 87 exceeded Q_{R0} on only 3 days between 1970 and 2020, whereas Q_{R0} was exceeded on 455 days between 1880 and 1930 (Jay and Naik 2011).

Baroclinic effects somewhat limit the validity of this analysis in the Columbia within about 5–15 km of the mouth, because the estuary is highly stratified within this reach during periods of large river discharge when x_{min} is shifted this far downstream (Jay and Smith 1990). Moreover, river discharge through the estuary is split between the north and south channel downstream of Rkm 40, with the portion of flow through the south channel decreasing as river discharge increases (Al-bahadily 2020), which may also modulate the relationship between x_{min} *and* Q_R. The theory still provides additional insight on the factors controlling deposition in an estuary, however. While the traditional perspective has been that the ETM of the LCRE forms by gravitational circulation (Gelfenbaum 1983) and tidal asymmetry (Jay and Simenstad 1996; Jay et al. 2007), the bed stress minimum caused by the interplay of tidal and river currents may also be important. Indeed, sand accumulation in the estuary occurs most rapidly near the upstream end of the energy flux divergence minimum (~Rkm 50), upstream of all salinity intrusion (Jay et al. 1990), and near the average location for the bed stress minimum (Fig. 11). Because the material trapped by the bed stress minimum travels as bed load, rather than the suspended load that makes the ETM, a wider gradation of material can also become deposited. That is, when river discharge is large enough, and x_{min} is shifted downstream near the salt wedge, greater volumes and gradations of material can become trapped in the ETM than would otherwise occur without a local minimum in bed stress. Indeed, the ETM of the LCRE is sand-bedded with long-term trapping of fines occurring in peripheral areas, on neaps, and during the low-flow season (Jay et al. 2007).

Creating and maintaining deeper water in the LCRE navigation channel have been achieved in large part through the construction of pile dikes and artificial islands throughout the river, and so the river has become narrower in many places as well as deeper. For example, pile dikes at Henrici Bar (~Rkm 145) decreased the river width from about 1400 m in 1909 to 870 m in 1959 (Hickson 1961). Reduction of river widths near the upstream boundary of a tidal river (B1) may counteract upstream migration of x_{min} due to channel deepening and flow reduction (see Fig. 8c) and may also enhance deposition upstream of x_{min} due to stronger spatial gradients in bed stress. Changes in river width are less studied than changes in depth but have been shown to contribute to changes in tides and river flow velocities (e.g., Talke et al. 2021). The theory presented here suggests that width alterations could play an important role in the sediment transport patterns controlled by the bed stress minimum for systems like the LCRE. Further exploration of the influence of river width is beyond the scope of this study but could provide additional insights to how channel improvement structures and land reclamation have altered sand deposition in the LCRE.

Delaware Estuary

Like the Columbia River, the Delaware Estuary contains a region with anomalously high shoaling rates. Roughly 60% of all material dredged from the Philadelphia-Sea shipping channel is derived from the Marcus Hook–New Castle reach around

Rkm 105 to 130 (Sommerfield et al. 2003). This region also coincides with a distinct down-estuary transition in bed composition from coarse to fine grain material that occurs between Rkm 120 to 140 (Sommerfield et al. 2003). Together, these depositional patterns imply that the system energy decreases as one moves downstream through this reach. Indeed, x_{min} occurs near Rkm 120 on average (Fig. 12b), and near Rkm 95 during peak spring discharge (QR = 2, 500 m^3 s^{-1}), which is also near where the tidally averaged bottom current is zero (Sommerfield and Wong 2011).

Channel development up to Rkm 200 has increased mean water depths in the Delaware Estuary from about 5 m in 1848 to 8 m in 2014 (DiLorenzo et al. 1993; Pareja-Roman et al. 2020). As a result, the calculated bed stress minimum location has moved upstream 10 km on average (Fig. 12b) and 15 km during peak spring discharge. Increased water depths have also decreased bed stress magnitudes and relaxed spatial gradients in bed stress upstream of x_{min} (Fig. 12a). Along-channel bed stress profiles even drop below the critical value of τ_c for medium-coarse sand mobility (D50 = 0.5 mm) during average spring season discharge ($Q_R \leq 600$ m^3 s^{-1}), hinting at a zone of limited mobility and temporary storage of medium sands. Indeed, most of the sediment delivered to the estuary turbidity maximum (ETM) likely originates from bed storage within the tidal freshwater river reach that extends from roughly Rkm 150 to 200 (Sommerfield and Wong 2011). Material likely accumulates upstream of x_{min} during low flows until river discharge increases enough to generate bed stresses greater than τc through the bed stress minimum. According to Eq. (16), this threshold occurs when $Q_R \geq 600$ m^3 s^{-1} for H = 8 m, but when $Q_R \geq 375$ m^3 s^{-1} under historical channel depths. The deposition zone also spans a longer stretch of the river presently than was the case in the nineteenth century. During low river discharge ($Q_R = 330$ m^3 s^{-1}), τ_{ebb} is less than τ_c between Rkm 118 and 206 when H = 8 m but between Rkm 127 and 163 when H = 5 m (Fig. 12a). In other words, the Delaware Estuary now likely stores a larger volume of sediment over a greater area that requires higher river discharge to disperse than was the case before the channel was deepened.

Hudson River

The Hudson River also features seasonal storage of sediment in the tidal-freshwater reach and down-river fining of bed composition. Ralston and Geyer (2017) note that the tidal freshwater reach of the river (upstream of Poughkeepsie, ~Rkm 120) traps about 40% of the sediment input from the watershed. Measurements by Nitsche et al. (2007) highlight a downstream fining of grain size from fluvially sourced sand/gravel to mud between roughly Rkm 200 and Rkm 100. Indeed, x_{min} is close to Rkm 150 during spring freshet conditions ($Q_R = 2000$ m^3 s^{-1}) (Fig. 13a), and over the past 20 years, the minimum value for xmin is estimated at about 110 km on 29th of August 2011. Furthermore, bed stress profiles in the Hudson River imply convergent sediment fluxes upstream of x_{min} during higher river discharge ($Q_R >$ 1000m^3 s^{-1}) and little to no transport of medium sand (D_{50} = 0.3 mm) upstream of Rkm 200 during lower river discharge ($Q_R \approx 100$ m^3 s^{-1}). Thus, sediments are likely trapped upstream of x_{min} due to convergent sediment fluxes during high discharge, with the coarser fraction ($D_{50} \geq 0.3$ mm) also experiencing limited transport during low discharge where τ_{ebb} drops below τ_c.

Up to Rkm 240, the Hudson River has been deepened from about 7 to 10 m between 1860 and 2015 (Ralston et al. 2019), which has moved the bed stress minimum calculated

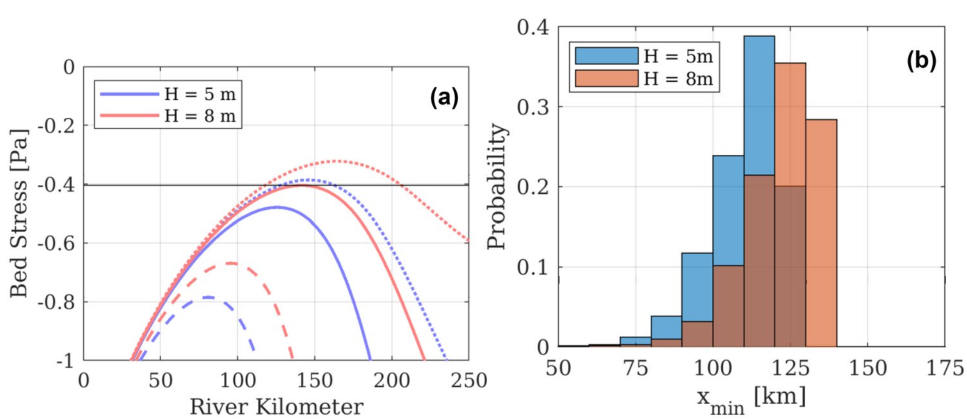

Fig. 12 Left: Bed stress profiles (Eq. (16)) in idealized Delaware Estuary for river discharge of 330 (dotted lines), 600 (solid lines), and 2500 (dashed lines) m^{3}s^{-1} assuming historical (blue lines) and contemporary channel depths (red lines). Solid black line denotes critical bed stress for movement of medium-coarse sand (D_{50} = 0.5 mm). Right: Delaware Estuary x_{min} as calculated using Eq. (20) using river discharge measurements > 330 m^{3}s^{-1} collected between 2000 and 2020 at USGS Station 01463500 (~Rkm 200)

by Eq. (20) upstream about 20 km. For example, the average value for x_{min} has increased from 150 to 170 km (Fig. 13b). Increased water depths have also reduced bed stress magnitudes upstream of the bed stress minimum in the Hudson River, which may have reduced the trapping efficiency upstream of x_{min} during higher river discharge.

Due to climate change, water withdrawal, and flow regulation, river discharge in the Hudson River during the spring freshet has decreased by about 17% (Ralston et al. 2019). Assuming a spring freshet discharge of 2400 m^3 s^{-1} puts the bed stress minimum close to Rkm 120 under historical channel depths (Eq. (20)). When Q_R equals 2000 m^3 s^{-1} and H equals 7 m, the x_{min} estimate resides near Rkm 130 (Fig. 13a). Thus, the bed stress minimum location during the freshet has likely moved upstream by about 20 km due to channel deepening and another 10 km due to changes in river discharge. Especially with the Hudson, natural variations in depth are substantial, and the river can be much deeper than the average (Nitsche et al. 2007); hence, localized, geometrically fixed hotspots of deposition may occur. Therefore, the upstream x_{min} shift suggested by theory should be interpreted as a general tendency, rather than an absolute.

Further Considerations

The above examples may underestimate historical shifts in x_{min}, because the tidal amplification observed in many deepened estuaries and flow-regulated rivers (Chernetsky et al. 2010; Winterwerp et al. 2013; Al-bahadily 2020; Talke and Jay 2020; Pareja-Roman et al. 2020) is not considered. As hypothesized in the "Introduction", an increase in tidal velocity U_{T0} (or decrease in tidal damping p) will increase x_{min} (Fig. 8a), which could lead to greater discrepancies between historical and modern x_{min} positions. Likewise, increased tidal velocities during spring tides will shift x_{min} further upstream than during neap tides, but the neap/spring shift will attenuate under larger river discharges. Further insight into the effects of tidal interactions on x_{min} is limited using the theory developed herein because only one tidal constituent is considered. The introduction of additional constituents at the ocean boundary will alter the functional form of the Fourier coefficients (Eqs. (7) and (8)), so a new relationship between x_{min} and forcing variables must be developed. Such an endeavor is beyond the scope of this paper but would provide a worthwhile complement to the results described above–especially for mixed-semidiurnal systems like the LCRE, which can produce tidal asymmetries through the interaction between semidiurnal and diurnal constituents (Hoitink et al. 2003; Nidzieko 2010).

The evaluation in this paper focuses on the bed stress during ebb because it is assumed that this is the most energetic time period with the strongest likelihood of significant transport (Eq. (16)). However, Aubrey and Speer (1985) demonstrate that certain U_T and U_4 phase differences produce flood-dominant currents, which can control the direction of transport and fate of sediments in an estuary. There are two river discharge thresholds to consider in this regard:

1. Moderate/strong river discharge ($U_R > U_4$) wherein the velocity is ebb dominant regardless of the phase difference between U_T and U_4. In fact, phase relations which produce flood-dominant tidal velocity ($U_T + U_4$) will, under these circumstances, produce ebb-dominant total velocity ($U_T + U_4 + U_R$) in both magnitude and duration.
2. Low river discharge ($U_R < U_4$) wherein ebb-flood dominance depends on phase difference between U_T and U_4.

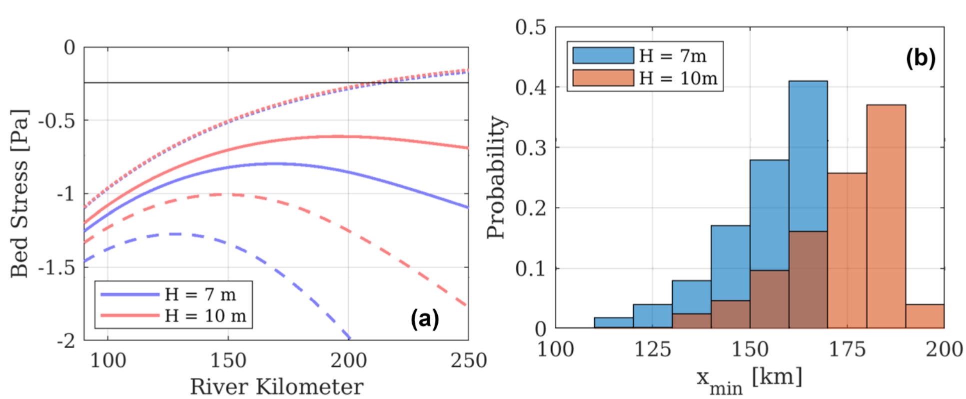

Fig. 13 Left: Bed stress profiles (Eq. (16)) in idealized Hudson River Estuary for river discharge of 100 (dotted lines), 1000 (solid lines), and 2000 (dashed lines) m^{3}s^{-1} assuming historical (blue lines) and contemporary channel depths (red lines). Solid black line denotes critical bed stress for movement of medium sand (D_{50} = 0.3 mm). Right: Hudson River Estuary x_{min} as calculated using Eq. (20) using river discharge measurements > 1000 m^{3}s^{-1} collected between 2000 and 2020 at USGS Station 01358000 (~Rkm 240). In this figure, the river is evaluated upstream of Newburgh (~Rkm 90) in order to honor the assumption of a convergent channel in the derivation of Eq. (20)

Thus, the assumption that the maximum bed stress occurs during ebb, regardless of U_T and U_4 phase difference, requires that $U_R > U_4$. This condition is satisfied in the Columbia River for $Q_R > 2000$ m^3 s^{-1} and in the Hudson River for $Q_R > 1000$ m^3 s^{-1}. Coincidentally these two discharge thresholds are the same for the development of a bed stress minimum. In other words, if $Q_R < 2000$ m^3 s^{-1} in the LCRE, then no bed stress minimum occurs. Thus, the ebb-dominant assumption fails only when there is no bed stress minimum to examine.

The Delaware River is different from the other two examples because its cross-section is much larger, and $U_R < U_4$ near and downstream of x_{min} for all discharge conditions. In addition U_T and U_4 are roughly in phase upstream of Rkm 40 (Pareja-Roman et al. 2020). Therefore, below x_{min} the maximum velocity occurs on flood tide not ebb. Upstream of x_{min}, however, $U_R > U_4$ and the total velocity is ebb dominant. Thus, x_{min} occurs near the transition between ebb-dominant currents upstream and flood-dominant currents downstream. The convergence in the velocity field set up by tidal asymmetry traps sediment and is augmented by the bed stress minimum.

The motivation for this study stemmed from observations of high volumes of sediment deposition in the Lower Columbia River FNC within the energy dissipation (bed stress) minimum reach. The analytical development provides insight into how the bed stress minimum migrates according to river discharge and channel geometry, yet further study of how this relationship manifests in the sediment transport patterns is warranted. While AdH simulations and bed stress profiles (Eq. (16)) suggest sediment accumulation near x_{min} due to convergent sediment fluxes, the magnitude of deposition cannot be specified based solely on the considerations discussed in this paper. Guo et al. (2014) employed a 1-D hydrodynamic model to examine the equilibrium bed elevation in the Yangtze estuary and found the upper reaches of the river to favor aggradation during high river discharge, resulting in shoaling on the order of 2–3 m over the course of several hundred years between approximately Rkm 200 and 550. Using the parameters outlined in their study, Eqs. (21) and (16) estimate a bed stress minimum at Rkm 150, with convergent sediment fluxes extending 300 km upstream of that point, which suggests a link between the bed stress minimum and long-term deposition patterns. Bed stress profiles imply that more material becomes trapped near the bed stress minimum as x_{min} decreases, but further research is needed in order to better understand the depositional consequences for changes in x_{min}.

Bed stress profiles in systems with strong topography exhibited a bed stress maximum upstream of x_{min} (Fig. 4b). Together, the location and magnitude of the bed stress minimum and maximum scale the sediment flux convergence upstream of x_{min}, and so further study of the bed stress maximum could help clarify how changes in channel depth and river discharge influence sediment deposition in tidal rivers. The bed stress maximum was observed in areas where U_R dominated currents near the bed (Fig. 5b) and apparently resulted from opposing gradients in river width and river depth. While Eq. (16) leads to an implicit formula for x_{min}, $4/\pi\, U_T^2 - 7/\pi\, U_R^2$, it is not capable of producing a bed stress maximum because the tidal frequency bed stress is overestimated as U_R/U_T grows larger (Fig. 2). Investigation of the bed stress maximum could be carried out using different approximations to a_2 and a_0 or perhaps a numerical approach defining x_{min}.

Observations by Friedrichs (1995) in 26 tidal systems imply that the bed stress in an alluvial system will uniformly tend towards a single value, the stability shear stress τ_s that maintains a zero gradient in the net along-channel sediment transport. What does this mean for the theory evaluated herein, where the existence of a bed stress minimum and maximum requires along-channel variation in bed stress? It means that a constant depth, width-convergent tidal river is out of equilibrium with regard to the spatial distribution of bed stress and will continually accrete material near the bed stress minimum in order to establish spatially uniform sediment transport (cf. Bolla Pittaluga et al. 2015). This result has profound implications for managing dredged material in alluvial tidal rivers, which have been progressively modified to emulate a constant depth channel to accommodate large container vessels. Moreover, there are also many systems that are not alluvial, where hard-rock topography and/or manmade structures limit the ability of the system to adjust towards a stable profile; some reaches of the LCRE are in this category. Such systems are also likely to need continual dredging.

Summary and Conclusions

Long-term trends in sediment transport have substantial implications for managing ecosystems and infrastructural investments in rivers. The spatial distribution of bed stress in tidal rivers that controls sand transport exhibits system scale patterns that manifest through non-linear interactions between tides and river discharge. The non-linear interactions between tidal forcing and river flow can lead to a bed stress minimum, which has previously been identified as a contributing factor to persistent, anomalous sand accumulation in the lower reaches of the Columbia River (Jay et al. 1990). Together with local topographic controls on bed stress (not discussed here), the variations in tidal forcing and river flow produced conditions for deposition of sand throughout the estuary/tidal river domain, sometimes far upstream of salinity intrusion and the traditional estuary turbidity maximum.

In this study, a Fourier series decomposition of the bed stress was used to develop an expression for how changes to river discharge and channel geometry influence the location of the bed stress minimum (x_{min}). While x_{min} was found to be topographically fixed by the channel convergence length scale, factors increasing river velocity shift x_{min} downstream, and those increasing tidal velocity shift x_{min} upstream. We note that flow regulation and channel deepening work together to move x_{min} upstream, suggesting that the locus of sand deposition has migrated as rivers have been progressively modified.

The theory developed herein was applied to idealized geometries approximating the Lower Columbia River, the Delaware River, and the Hudson River. Because of differences in channel geometry and river discharge, these systems display a wide range of sediment transport behavior associated with the bed stress minimum. In particular, they differ in the importance of river flow. In rivers with higher river velocity (like the LCRE), $|\tau_{ebb}|$ is everywhere greater than τ_c, while in lower velocity rivers like the Delaware River, $|\tau_{ebb}(x)| \sim \tau_c$. The Hudson is intermediate between the other two systems. Analytical representations of bed stress profiles and x_{min} in these systems suggest:

- The locus of deposition is determined primarily by spatial gradients in bed stress in alluvial systems with higher river velocity and by transport thresholds in lower velocity rivers. In the former, deposition peaks during high river discharge when gradients in bed stress are greatest, and in the latter, deposition can increase during lower river discharge when τ_{ebb} drops below τ_c.
- In high river velocity systems like the Columbia, a river discharge threshold Q_{R0} exists, above which x_{min} can be exported to the ocean, feeding sediment to the littoral system. Flow regulation can decrease the frequency of such events.
- Transport thresholds in lower velocity rivers likely manifest as seasonal storage of sediments in the upper river that disperse when river discharge is large enough. Channel deepening has apparently increased the frequency and spatial extent of storage in the tidal-freshwater reach of the Delaware Estuary.
- Channel deepening leads to decreased bed stress magnitudes and bed stress gradients, which may decrease shoaling upstream of x_{min} in high velocity rivers, yet increase shoaling in low velocity rivers.
- Down-river fining of bed material features prominently in low-velocity rivers because $|\tau_{ebb}(x)| \sim \tau_c$. This can be particularly important in governing the substrate composition of in-water habitats and should be considered when evaluating the influence of climate change and anthropogenic activities on habitat quality.

Supplementary Information The online version contains supplementary material available at https://doi.org/10.1007/s12237-022-01156-9.

Acknowledgements Upon acceptance of this paper, water level and flow data used in this study will be archived by the Portland State University Library (https://pdxscholar.library.pdx.edu/cengin_data/).

Funding Stefan Talke's work on this paper was supported by NSF Grant 2013280.

References

Al-bahadily, A. 2020. *Long term changes to the Lower Columbia River Estuary (LCRE) hydrodynamics and salinity patterns*. Portland State University.

Allen, G.P., et al. 1980. Effects of tides on mixing and suspended sediment transport in macrotidal estuaries. *Sedimentary Geology* 26 (1–3): 69–90.

Aubrey, D.G., and P.E. Speer. 1985. A study of non-linear tidal propagation in shallow inlet/estuarine systems Part 1: Observations. *Estuarine, Coastal and Shelf Science* 21: 185–205.

Bolla Pittaluga, M., N. Tambroni, A. Canestrelli, R. Slingerland, S. Lanzoni, and G. Seminara. 2015. Where river and tide meet: The morphodynamic equilibrium of alluvial estuaries. *Journal of Geophysical Research: Earth Surface* 120 (1): 75–94.

Branch, R.A., et al. 2021. Surface turbulence reveals riverbed drag coefficient. *Geophysical Research Letters* 48 (10): e2020GL092326.

Burchard, H., and H. Baumert. 1998. The formation of estuarine turbidity maxima due to density effects in the salt wedge. A hydrodynamic process study. *Journal of Physical Oceanography* 28 (2): 309–321.

Burchard, H., H.M. Schuttelaars, and D.K. Ralston. 2018. Sediment trapping in estuaries. *Annual Review of Marine Science* 10: 371–395.

Buschman, F.A., A.J.F. Hoitink, M. Van Der Vegt, and P. Hoekstra. 2009. Subtidal water level variation controlled by river flow and tides. *Water Resources Research* 45: 10.

Chant, R.J., D. Fugate, and E. Garvey. 2011. The shaping of an estuarine superfund site: Roles of evolving dynamics and geomorphology. *Estuaries and Coasts* 34 (1): 90–105.

Chatanantavet, P., M.P. Lamb, and J.A. Nittrouer. 2012. Backwater controls of avulsion location on deltas. *Geophysical Research Letters* 39: 1.

Chernetsky, A.S., H.M. Schuttelaars, and S.A. Talke. 2010. The effect of tidal asymmetry and temporal settling lag on sediment trapping in tidal estuaries. *Ocean Dynamics* 60 (5): 1219–1241.

Dalrymple, R.W., B.A. Zaitlin, and R. Boyd. 1992. Estuarine facies models; conceptual basis and stratigraphic implications. *Journal of Sedimentary Research* 62 (6): 1130–1146.

de Jonge, V.N., H.M. Schuttelaars, J.E. van Beusekom, S.A. Talke, and H.E. de Swart. 2014a. The influence of channel deepening on estuarine turbidity levels and dynamics, as exemplified by the Ems estuary. *Estuarine, Coastal and Shelf Science* 139: 46–59.

Dijkstra, Y.M., H.M. Schuttelaars, and H. Burchard. 2017. Generation of exchange flows in estuaries by tidal and gravitational eddy viscosity-shear covariance (ESCO). *Journal of Geophysical Research, Oceans* 122 (5): 4217–4237.

Dijkstra, Y.M., H.M. Schuttelaars, G.P. Schramkowski, and R.L. Brouwer. 2019. Modeling the transition to high sediment concentrations as a response to channel deepening in the Ems River Estuary. *Journal of Geophysical Research, Oceans* 124 (3): 1578–1594.

DiLorenzo, J.L., P. Huang, M.L. Thatcher, and T.O. Najarian. 1993. *Dredging impacts on Delaware Estuary tides*, 86–104. Estuarine and Coastal Modeling: ASCE.

Dronkers, J.J. 1964. *Tidal computations in rivers and coastal waters*. North-Holland Publishing Company.

Dyer, K. 1986. *Coastal and estuarine sediment dynamics*. John Wiley and Sons.

Dyer, Keith R. 1995. Sediment transport processes in estuaries. *Developments in Sedimentology* 53: 423–449.

Elias, E.P., G. Gelfenbaum, and A.J. Van der Westhuysen. 2012. Validation of a coupled wave-flow model in a high-energy setting: the mouth of the Columbia River. *Journal of Geophysical Research Oceans* 117 (C9).

EPA. 2014. *Record of decision, Lower Duwamish Waterway Superfund Site*.

EPA. 2016. *Record of decision, Lower 8.3 Miles of the Lower Passaic River Part of the Diamond Alkali Superfund Site Essex and Hudson Counties, New Jersey*.

EPA. 2017. *Record of decision, Portland Harbor Superfund Site Portland, Oregon*.

Familkhalili, R., S.A. Talke, and D.A. Jay. 2022. Compound flooding in convergent estuaries: insights from an analytical model. *Ocean Science Discussions* 18 (4): 1203–1220.

Festa, J.F., and D.V. Hansen. 1978. Turbidity maxima in partially mixed estuaries: A two-dimensional numerical model. *Estuarine and Coastal Marine Science* 7 (4): 347–359.

Friedrichs, C.T. 1995. Stability shear stress and equilibrium cross-sectional geometry of sheltered tidal channels. *Journal of Coastal Research* 11: 1062–1074.

Friedrichs, C.T., and D.G. Aubrey. 1994. Tidal propagation in strongly convergent channels. *Journal of Geophysical Research: Oceans* 99 (C2): 3321–3336.

Friedrichs, C.T., B.A. Armbrust, and H.E. deSwart. 1998. Hydrodynamics and equilibrium sediment dynamics of shallow, funnel-shaped tidal estuaries. *VIMS Books and Book Chapters* 38.

Gelfenbaum, G. 1983. Suspended-sediment response to semidiurnal and fortnightly tidal variations in a mesotidal estuary: Columbia River, USA. *Marine Geology* 52 (1–2): 39–57.

Geyer, W.R. 1993. The importance of suppression of turbulence by stratification on the estuarine turbidity maximum. *Estuaries* 16 (1): 113–125.

Giese, B.S., and D.A. Jay. 1989. Modelling tidal energetics of the Columbia River estuary. *Estuarine, Coastal and Shelf Science* 29 (6): 549–571.

Godin, G. 1991. Compact approximations to the bottom friction term, for the study of tides propagating in channels. *Continental Shelf Research* 11 (7): 579–589.

Godin, G., et al. 1991. Frictional effects in river tides. *Tidal hydrodynamics* 379–402.

Guo, L., et al. 2014. The role of river flow and tidal asymmetry on 1-D estuarine morphodynamics. *Journal of Geophysical Research, Earth Surface* 119 (11): 2315–2334.

Haberman, R. 2004. *Applied partial differential equations with Fourier series and boundary value problems*. Pearson Prentice Hall.

Helaire, L.T., S.A. Talke, D.A. Jay, and D. Mahedy. 2019. Historical changes in Lower Columbia River and estuary floods: A numerical study. *Journal of Geophysical Research: Oceans* 124 (11): 7926–7946. https://doi.org/10.1029/2019JC015055.

Hickson, R.E. 1930. Shoaling on the lower Columbia River. *The Military Engineer* 22 (123): 217–219.

Hickson, R.E. 1961. Columbia River ship channel improvement and maintenance. *Journal of the Waterways and Harbors Division* 87 (3): 71–94.

Hoitink, A.J.F., and D.A. Jay. 2016. Tidal river dynamics: Implications for deltas. *Reviews of Geophysics* 54 (1): 240–272.

Hoitink, A.J.F., P. Hoekstra, and D.S. van Maren. 2003. Flow asymmetry associated with astronomical tides: Implications for the residual transport of sediment. *Journal of Geophysical Research* 108: C10.

Huijts, K.M.H., H.M. Schuttelaars, H.E. De Swart, and C.T. Friedrichs. 2009. Analytical study of the transverse distribution of along-channel and transverse residual flows in tidal estuaries. *Continental Shelf Research* 29 (1): 89–100.

Ianniello, J.P. 1979. Tidally induced residual currents in estuaries of variable breadth and depth. *Journal of Physical Oceanography* 9 (5): 962–974.

Jay, D.A. 1991. Green's law revisited: Tidal long-wave propagation in channels with strong topography. *Journal of Geophysical Research* 96 (C11): 20585–20598.

Jay, D.A., and J.D. Musiak. 1994. Particle trapping in estuarine tidal flows. *Journal of Geophysical Research* 99 (C10): 20445–20461.

Jay, D.A., and P. Naik. 2011. Distinguishing human and climate influences on hydrological disturbance processes in the Columbia River, USA. *Hydrological Sciences Journal* 56: 1186–1209.

Jay, D.A., and C.A. Simenstad. 1996. Downstream effects of water withdrawal in a small, high-gradient basin: Erosion and deposition on the Skokomish River Delta. *Estuaries* 19: 501–517.

Jay, D.A., and J.D. Smith. 1990. Circulation, density distribution and neap-spring transitions in the Columbia River Estuary. *Progress in Oceanography* 25: 81–112.

Jay, D.A., B.S. Giese, and C.R. Sherwood. 1990. Energetics and sedimentary processes in the Columbia River Estuary. *Progress in Oceanography* 25: 157–174.

Jay, D.A., P.M. Orton, T. Chisholm, D.J. Wilson, and A.M.V. Fain. 2007. Particle trapping in stratified estuaries – I Consequences of mass conservation and explorations of a parameter space. *Estuaries and Coasts* 30: 1095–1105.

Jay, D.A., S.A. Talke, A. Hudson, and M. Twardowski. 2015. Estuarine turbidity maxima revisited: Instrumental approaches, remote sensing, modeling studies, and new directions. In *Fluvial-Tidal Sedimentology, Developments in Sedimentology*, vol. 68, ed. P.J. Ashworth, J.L. Best, and D.R. Parsons, 49–109. Elsevier.

Jay, D.A., A. Borde, and H. Diefenderfer. 2016. Tidal-fluvial and estuarine processes in the Lower Columbia River: II: Water level models, inundation, reach classification and vegetation. *Estuaries and Coasts* 39: 1299–1324. https://doi.org/10.1007/s12237-016-0082-4.

Kaminsky, G.M., et al. 2010. Historical evolution of the Columbia River littoral cell. *Marine Geology* 273 (1–4): 96–126.

Lanzoni, S., and G. Seminara. 2002. Long-term evolution and morphodynamic equilibrium of tidal channels. *Journal of Geophysical Research: Oceans* 107 (C1): 1–1.

Meade, R.H. 1969. Landward transport of bottom sediments in estuaries of the Atlantic coastal plain. *Journal of Sedimentary Petrology* 39 (1): 222–234.

Naik, P., and D.A. Jay. 2010. Human and climate impacts on Columbia River hydrology and salmonids, *River Res. Applic.* 27: 1270–1276. https://doi.org/10.1002/rra.1422.

Naik, P.K., and D.A. Jay. 2011. Distinguishing human and climate influences on the Columbia River: Changes in mean flow and sediment transport. *Journal of Hydrology* 404 (3): 259–277.

Nidzieko, N.J. 2010. Tidal asymmetry in estuaries with mixed semidiurnal/diurnal tides. *Journal of Geophysical Research Oceans* 115 (C8).

Nitsche, F.O., et al. 2007. Regional patterns and local variations of sediment distribution in the Hudson River Estuary. *Estuarine, Coastal and Shelf Science* 71 (1–2): 259–277.

Nittrouer, J.A., J. Shaw, M.P. Lamb, and D. Mohrig. 2012. Spatial and temporal trends for water-flow velocity and bed-material

sediment transport in the lower Mississippi River. *Bulletin* 124 (3): 400–414.
NOAA tide and current predictions. https://tidesandcurrents.noaa.gov/map/index.html. Accessed 1 Sept 2021.
Pareja-Roman, L.F., R.J. Chant, and C.K. Sommerfield. 2020. Impact of historical channel deepening on tidal hydraulics in the Delaware Estuary. *Journal of Geophysical Research: Oceans* 125 (12): e2020JC016256.
Postma, H. 1961. Transport and accumulation of suspended matter in the Dutch Wadden Sea. *Netherlands Journal of Sea Research* 1 (1): 148–190.
Proudman, J. 1952. *Dynamical oceanography*. Dover.
Ralston, D.K., and W.R. Geyer. 2017. Sediment transport time scales and trapping efficiency in a tidal river. *Journal of Geophysical Research: Earth Surface* 122 (11): 2042–2063.
Ralston, D.K., S.A. Talke, W.R. Geyer, H.A.M. Al-Zubaidi, and C.K. Sommerfield. 2019. Bigger tides, less flooding: Effects of dredging on barotropic dynamics in a highly modified estuary. *Journal of Geophysical Research: Oceans* 124 (1): 196–211.
Savant, G., C. Berger, T.O. McAlpin, and J.N. Tate. 2011. Efficient implicit finite-element hydrodynamic model for dam and levee breach. *Journal of Hydraulic Engineering* 137 (9): 1005–1018.
Savenije, H.H. 2005. *Salinity and tides in alluvial estuaries*. Gulf Professional Publishing.
Sherwood, C.R., D.A. Jay, R.B. Harvey, P. Hamilton, and C.A. Simenstad. 1990. Historical changes in the Columbia River estuary. *Progress in Oceanography* 25 (1): 299–352.
Sommerfield, C.K., and K. Wong. 2011. Mechanisms of sediment flux and turbidity maintenance in the Delaware Estuary. *Journal of Geophysical Research: Oceans* 116 (C1).
Sommerfield, C.K., J.A. Madsen, and P. Hall. 2003. *Sedimentological and geophysical survey of the upper Delaware estuary*. Delaware River Basin Commission Final report.
Speer, P.E., and D.G. Aubrey. 1985. A study of non-linear tidal propagation in shallow in- let/estuarine systems part 2: Theory. *Estuarine, Coastal and Shelf Science* 21: 207–224.
Talke, S.A., and D.A. Jay. 2020. Changing tides: The role of natural and anthropogenic factors. *Annual Review of Marine Science* 12: 121–151.
Talke, S.A., H.E. de Swart, and H.M. Schuttelaars. 2009a. Feedback between residual circulations and sediment distribution in highly turbid estuaries: An analytical model. *Continental Shelf Research* 29 (1): 119–135.
Talke, S.A., H.E. de Swart, and V. de Jonge. 2009b. An idealized model and systematic process study of oxygen depletion in highly turbid estuaries. *Estuaries and Coasts* 32 (4): 602–620.
Talke, S.A., R. Familkhalili, and D.A. Jay. 2021. The influence of channel deepening on tides, river discharge effects, and storm surge. *Journal of Geophysical Research: Oceans* 126 (5): e2020JC016328.
Templeton, W.J., and D.A. Jay. 2012. Lower Columbia River sand supply and removal: Estimates of two sand budget components. *Journal of Waterway, Port, Coastal, and Ocean Engineering* 139 (5): 383–392.
USACE. 2020. *USACE RSM Program Update*. https://rsm.usace.army.mil/techtransfer/FY20/RSM-IPR-Aug2020/briefs/1_01_2020_RSM_ERDC_ProgramUpdate.pdf. Accessed 4 Aug 2021.
Winterwerp, J.C., Z.B. Wang, A. Van Braeckel, G. Van Holland, and F. Kösters. 2013. Man-induced regime shifts in small estuaries–II: A comparison of rivers. *Ocean Dynamics* 63 (11): 1293–1306.